

INFORMATION TO USERS

This manuscript has been reproduced from the microfilm master. UMI films the text directly from the original or copy submitted. Thus, some thesis and dissertation copies are in typewriter face, while others may be from any type of computer printer.

The quality of this reproduction is dependent upon the quality of the copy submitted. Broken or indistinct print, colored or poor quality illustrations and photographs, print bleedthrough, substandard margins, and improper alignment can adversely affect reproduction.

In the unlikely event that the author did not send UMI a complete manuscript and there are missing pages, these will be noted. Also, if unauthorized copyright material had to be removed, a note will indicate the deletion.

Oversize materials (e.g., maps, drawings, charts) are reproduced by sectioning the original, beginning at the upper left-hand corner and continuing from left to right in equal sections with small overlaps.

Photographs included in the original manuscript have been reproduced xerographically in this copy. Higher quality 6" x 9" black and white photographic prints are available for any photographs or illustrations appearing in this copy for an additional charge. Contact UMI directly to order.

**ProQuest Information and Learning
300 North Zeeb Road, Ann Arbor, MI 48106-1346 USA
800-521-0600**

UMI[®]

University of Alberta

**Particle Image Velocimetry
Applied to a Deflected Wall Jet**

by

Peter Onyshko



A thesis submitted to the Faculty of Graduate Studies and Research in
partial fulfillment of the requirements for the degree of Master of Science
in

Water Resources Engineering

Department of Civil and Environmental Engineering

Edmonton, Alberta

Spring 2002



**National Library
of Canada**

**Acquisitions and
Bibliographic Services**

**395 Wellington Street
Ottawa ON K1A 0N4
Canada**

**Bibliothèque nationale
du Canada**

**Acquisitions et
services bibliographiques**

**395, rue Wellington
Ottawa ON K1A 0N4
Canada**

Your file Votre référence

Our file Notre référence

The author has granted a non-exclusive licence allowing the National Library of Canada to reproduce, loan, distribute or sell copies of this thesis in microform, paper or electronic formats.

The author retains ownership of the copyright in this thesis. Neither the thesis nor substantial extracts from it may be printed or otherwise reproduced without the author's permission.

L'auteur a accordé une licence non exclusive permettant à la Bibliothèque nationale du Canada de reproduire, prêter, distribuer ou vendre des copies de cette thèse sous la forme de microfiche/film, de reproduction sur papier ou sur format électronique.

L'auteur conserve la propriété du droit d'auteur qui protège cette thèse. Ni la thèse ni des extraits substantiels de celle-ci ne doivent être imprimés ou autrement reproduits sans son autorisation.

0-612-69746-0

Canada

University of Alberta

Library Release Form

Name of Author: Peter Onyshko

Title of Thesis: Particle Image Velocimetry Applied to a Deflected Wall Jet

Degree: Master of Science

Year this Degree Granted: 2002

Permission is hereby granted to the University of Alberta Library to reproduce single copies of this thesis and to lend or sell such copies for private, scholarly or scientific research purposes only.

The author reserves all other publication and other rights in association with the copyright in the thesis, and except as herein provided, neither the thesis nor any substantial portion thereof may be printed or otherwise reproduced in any material form whatever without the author's prior written permission.

Peter Onyshko.

8307 - 44 Avenue, Edmonton, Alberta

15 april 2002

University of Alberta

Faculty of Graduate Studies and Research

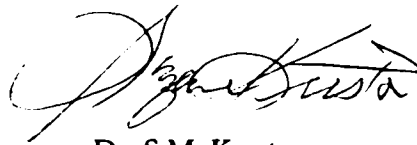
The undersigned certify that they have read, and recommended to the Faculty of Graduate Studies and Research for acceptance, a thesis entitled Particle Image Velocimetry Applied to a Deflected Wall Jet submitted by Peter Onyshko in partial fulfillment of the requirements for the degree of Master of Science in Water Resources Engineering.



Dr. M.R. Loewen



Dr. N. Bajaratnam



Dr. S.M. Kresta

12 april 2002

Abstract

This thesis presents the results of an experimental study of a deflected wall jet using particle image velocimetry (PIV). A wall jet was formed in a rectangular flume and deflected upwards to the water surface by a baffle affixed across the width of the flume. A square data mosaic was assembled from fourteen tesserae, each with 15 cm square fields of view. The velocity data was decomposed and the following flow parameters were calculated: u and v velocities, kinetic energy, Reynolds stress, turbulent kinetic energy, dissipation rate, vorticity, strain and Kolmogorov length and velocity scales. Profiles along the curved jet trajectory were extracted and similarity analyses were performed. Wall jet-like, plane jet-like and surface jet-like regions of flow were identified. Results consistent with those of Wu and Rajaratnam (1995a) were observed for the mean flow. Turbulence was concentrated in the body of the jet and decayed with distance along the trajectory.

Acknowledgements

My sincere gratitude is extended to Dr. M.R. Loewen and Dr. N. Rajaratnam for their support, guidance and indulgence throughout the course of my research. I would also like to thank Perry Fedun for his assistance with my experimental arrangement.

I gratefully acknowledge the help provided by both my brother and my colleagues at the T. Blench Hydraulics Laboratory in the collection and analysis of data. My heartfelt appreciation is also extended to my immediate family and close friends for their continued encouragement and support.

Funding for this research was provided by the National Science and Engineering Research Council in the form of a postgraduate scholarship.

Table of Contents

1 Introduction	1
2 Literature Review	4
2.1 Plane Turbulent Jets	4
2.1.1 Classic Plane Jet	4
2.1.2 Plane Jet in a Crossflow	8
2.2 Plane Turbulent Wall Jets	9
2.3 Plane Turbulent Surface Jets	11
2.4 Plane Turbulent Deflected Wall Jets.....	12
3 Experimental Methods	20
3.1 PIV Methodology	20
3.2 Flume Arrangement	21
3.3 PIV Setup	22
3.3.1 Illumination Sub-System	22
3.3.2 Timing Sub-System	23
3.3.3 Imaging Sub-System.....	24
3.4 Measurement Programme	25
4 Data Processing.....	42
4.1 Image Pre-Processing	42
4.2 Primary PIV Processing.....	43
4.3 Corrective Post-Processing	44
4.4 Supplementary Processing.....	46
4.5 Error Consideration	48
4.5.1 Out-of-Plane Motion	48
4.5.2 Standard PIV Errors	49
4.5.3 Misalignment Errors	51
5 Data Analysis.....	68
5.1 Whole-Field Flow Properties	68
5.1.1 Mean Velocity.....	69
5.1.2 Mean Kinetic Energy	70
5.1.3 Mean Reynolds Stress.....	71
5.1.4 Mean Turbulent Kinetic Energy	73
5.1.5 Mean Dissipation	74
5.1.6 Vorticity	75
5.1.6.1 Mean Vorticity	75
5.1.6.2 Mean Circulation	77
5.1.6.3 Instantaneous Vorticity	78
5.1.7 Mean Strain.....	80
5.1.8 Mean Kolmogorov Scales.....	81

5.2 Jet Flow and Development	81
5.2.1 Trajectory Identification	82
5.2.2 Centreline Velocity Decay	85
5.2.3 Centreline Velocity Angles	87
5.2.4 Profile Extraction	88
5.2.5 Characteristic Length Scales	89
5.2.6 Nondimensional Similarity	92
5.2.6.1 Wall Jet-Like Flow	93
5.2.6.2 Plane Jet-Like Flow	94
5.2.6.3 Surface Jet-Like Flow	95
5.2.6.4 Return Surface Jet-Like Flow	96
5.2.6.5 Transition Flows	97
5.2.7 Discharge Intensity Variation	97
5.2.8 Momentum Flux Variation	100
5.2.9 Entrainment Velocities	101
6 Conclusion	216
6.1 Experimental Observations	216
6.2 Future Considerations	218
7 References	219
8 Appendix	223

List of Tables

Table 3.1: Global coordinate tesserae positions and extents.	27
Table 3.2: Mean water surface profile coordinates.	28
Table 3.3: Environmental parameters.....	29
Table 3.4: Experimental timing delays and separations.....	30
Table 4.1: Spurious vector statistics arranged by tessera and iteration.....	53
Table 4.2: Maximum displacement and velocity resolutions for all tesserae.	54
Table 4.3: Estimates of out-of-plane displacement (d_{pz}) for all tesserae.	55
Table 4.4: Peak locking error percentages (I_{plu} and I_{plv}) for all tesserae.	56
Table 4.5: Errors in velocity (e_u and e_v) for all tesserae.....	57
Table 4.6: Errors in vorticity (e_w) for all tesserae.	58
Table 5.1: Minimum and maximum mean velocities in each tessera.	102
Table 5.2: Minimum and maximum mean flow properties in the full data mosaic. ..	103
Table 5.3: Minimum and maximum mean flow properties in each tessera.	104
Table 5.4: Flow regime extents and boundary ordinates for the main jet flow.	108
Table 5.5: Flow regime extents and boundary ordinates for the return jet flow.	109
Table 5.6: Variation of the C_1 coefficient along the full jet trajectory.	110
Table 5.7: Variation of the C_2 coefficient for the negative profile stem (δ_{1-}) along the full jet trajectory.	111
Table 5.8: Variation of the C_2 coefficient for the positive profile stem (δ_{1+}) along the full jet trajectory.....	112
Table 5.9: Variation of the C_3 coefficient along the full jet trajectory.	113
Table 8.1: Contents of accompanying compact disc.....	224

List of Figures

Figure 1.1: Dye visualization still of the plane deflected wall jet.	3
Figure 2.1: Plane turbulent jet definition sketch.	14
Figure 2.2: Plane turbulent jet potential core and development sketch.	15
Figure 2.3: Plane turbulent jet in a crossflow definition sketch.	16
Figure 2.4: Plane turbulent wall jet definition sketch.	17
Figure 2.5: Plane turbulent surface jet definition sketch.	18
Figure 2.6: Plane turbulent deflected wall jet definition sketch.	19
Figure 3.1: Flume arrangement diagram.	31
Figure 3.2: Channel measured drawing.	32
Figure 3.3: (a) General PIV setup layout and (b) broad laser timing structure.	33
Figure 3.4: PIV illumination sub-system diagram.	34
Figure 3.5: (a) PIV timing sub-system signal flow and (b) detailed timing scheme.	35
Figure 3.6: PIV imaging sub-system target apparatus measured drawing.	36
Figure 3.7: T. Blench Hydraulics Laboratory experimental area.	37
Figure 3.8: Flume arrangement and PIV setup.	37
Figure 3.9: Flume arrangement pump and magnetic flowmeter.	38
Figure 3.10 :Flume arrangement water reservoir.	38
Figure 3.11: PIV illumination sub-system optical rail, lens and mirror.	39
Figure 3.12: PIV timing sub-system sync stripper and delay generator.	39
Figure 3.13: PIV imaging sub-system.	40
Figure 3.14: Submerged targeting apparatus and CDD camera.	40
Figure 3.15: Target images taken of (a) tessera 12 and (b) tessera 13.	41
Figure 4.1: Baffle shadow and edge reflection defects visible in (a) tessera 2 and (b) tessera 3 raw PIV images.	59
Figure 4.2: Water surface reflection defects visible in (a) tessera 6 and (b) tessera 7 raw PIV images.	60
Figure 4.3: Interrogation window grid superposed on a tessera 4 PIV image.	61
Figure 4.4: PIV methodology schematic showing (a) interrogation and search windows, (b) the correlation field and (c) identified pixel displacements.	62
Figure 4.5: Representative instantaneous raw pixel displacement vector fields for (a) tessera 4 and (b) tessera 7.	63
Figure 4.6: Exclusion zones in the assembled mosaic.	64
Figure 4.7: Representative instantaneous corrected and interpolated pixel displacement vector fields for (a) tessera 4 and (b) tessera 7.	65

Figure 4.8: Peak locking error in tessera 1 raw pixel displacement data.....	66
Figure 4.9: Example of edge dislocation in the upper-left corner of tessera 10.....	67
Figure 5.1: Full mean velocity vector field with additional superposed field showing every tenth vector at a larger scale.	114
Figure 5.2: Mean velocity vector field for full mosaic showing every tenth vector at scale and jet centreline trajectory.....	115
Figure 5.3: Mean velocity vector field of the area encompassing the small eddy of clockwise rotation.....	116
Figure 5.4: (a-b) Mean kinetic energy per unit mass (KE) contour maps describing full data mosaic with jet centreline trajectory.	117
Figure 5.5: Mean kinetic energy per unit mass (KE) contour map for tessera 3 with jet centreline trajectory.....	118
Figure 5.6: (a-b) Mean Reynolds stress per unit mass (τ/ρ) contour maps describing full data mosaic with jet centreline trajectory.....	119
Figure 5.7: Mean Reynolds stress per unit mass (τ/ρ) contour map for tessera 3 with jet centreline trajectory.	120
Figure 5.8: (a-b) Mean turbulent kinetic energy per unit mass (k) contour maps describing full data mosaic with jet centreline trajectory.....	121
Figure 5.9: Mean turbulent kinetic energy per unit mass (k) contour map for tessera 3 with jet centreline trajectory.	122
Figure 5.10: The cumulative average, plotted over increasing periods of time and averaging larger batches of PIV data files, of the sum of all turbulent kinetic energy (k) measurements in a tessera, presented for (a) tessera 2 and (b) tessera 4; showing that a sufficient amount of data was collected at each tessera for representative mean turbulent flow characteristics to be calculated. Note the stabilization by 2.5 minutes.	123
Figure 5.11: (a-b) Mean dissipation per unit mass (d) contour maps describing full data mosaic with jet centreline trajectory.....	124
Figure 5.12: Mean dissipation per unit mass (d) contour map for tessera 3 with jet centreline trajectory.....	125
Figure 5.13: (a-d) Mean vorticity (ω) contour maps describing full data mosaic with jet centreline trajectory.	126
Figure 5.14: Mean vorticity (ω) contour map of mosaic area surrounding the baffle.	128
Figure 5.15: Velocity, vorticity and circulation in the large elliptical eddy found on the inbound side of the jet centreline trajectory.	129

Figure 5.16: Vorticity distribution along the radius of the large elliptical eddy found on the inbound side of the jet centreline trajectory.....	130
Figure 5.17: Instantaneous vorticity (ω_i) contour map for tessera 2; consecutive 15 Hz frames with the background vorticity plotted in white to accentuate the coherent vortical structures and with the jet centreline trajectory as reference....	131
Figure 5.18: Instantaneous vorticity (ω_i) contour map for tessera 3; consecutive 15 Hz frames with the background vorticity plotted in white to accentuate the coherent vortical structures and with the jet centreline trajectory as reference....	133
Figure 5.19: Instantaneous vorticity (ω_i) contour map for tessera 1; consecutive 15 Hz frames with the background vorticity plotted in white to accentuate the coherent vortical structures.	135
Figure 5.20: Instantaneous vorticity (ω_i) contour map for tessera 11; consecutive 15 Hz frames with the background vorticity plotted in white to accentuate the coherent vortical structures.	137
Figure 5.21: (a-b) Mean strain (ϵ) contour maps describing full data mosaic with jet centreline trajectory.....	139
Figure 5.22: Mean strain (ϵ) contour map for tessera 3 with jet centreline trajectory.	140
Figure 5.23: Mean Kolmogorov (a) length scale (l_k) and (b) velocity scale (v_k) contour maps describing full data mosaic with jet centreline trajectory.....	141
Figure 5.24: Mean Kolmogorov (a) length scale (l_k) and (b) velocity scale (v_k) contour maps for tessera 3 with jet centreline trajectory.	142
Figure 5.25: Replacement of mean velocity vectors in water surface reflection defect exclusion zone with raw mean corrected and scaled velocity vectors.	143
Figure 5.26: Interpolated mean velocity vectors in baffle reflection and baffle shadow defect exclusion zone.	144
Figure 5.27: Locations of the maximum mean velocity magnitudes found in each column and each row of the full data mosaic.	145
Figure 5.28: The contour line showing where the mean vorticity (ω) is equal to zero in the full data mosaic, including the replacement vectors in the water surface reflection defect exclusion zone.	146
Figure 5.29: Final deflected wall jet trajectory for both the main jet and the return flow section.	147
Figure 5.30: Flow regimes within the plane deflected wall jet.	148
Figure 5.31: Variation of U_m with s over (a) the full jet trajectory and over (b-d) the sections upstream of the baffle, between the baffle and the point of impingement and downstream of the point of impingement, respectively.	149

Figure 5.32: Variation of U_m/U_o with $\xi^{-0.5}$ over (a) the full jet trajectory and over (b-d) the sections upstream of the baffle, between the baffle and the point of impingement and downstream of the point of impingement, respectively.	151
Figure 5.33: Variation of the C_1 coefficient along the full jet centreline trajectory.	153
Figure 5.34: Variation of (a) U_m with s and of (b) U_m/U_o with $\xi^{-0.5}$ along the full return flow jet trajectory.	154
Figure 5.35: Variation of θ_c with s over (a) the full jet trajectory and over (b-d) the sections upstream of the baffle, between the baffle and the point of impingement and downstream of the point of impingement, respectively.	155
Figure 5.36: Variation of θ_c with s along the full return flow jet trajectory.	157
Figure 5.37: Select mean velocity vector profiles showing the development of the plane deflected wall jet with a provided velocity scale; only every tenth mean velocity data point along each profile section is plotted for clarity.	158
Figure 5.38: Select mean velocity profiles showing the development of the plane deflected wall jet in the wall jet-like (WJL) region of flow.	159
Figure 5.39: Select mean velocity profiles showing the development of the plane deflected wall jet in the plane jet-like (PJL) region of flow.	160
Figure 5.40: Select mean velocity profiles showing the development of the plane deflected wall jet in the surface jet-like (SJL) region of flow.	161
Figure 5.41: Select mean velocity profiles showing the development of the plane deflected wall jet in the return flow surface jet-like (SJL) region; only every sixth mean velocity data point along each profile section is plotted for clarity. ...	162
Figure 5.42: Loci of the jet centreline trajectory, the jet half-width (δ_1), the jet width (δ_2) and the water surface in the global Cartesian coordinate system.	163
Figure 5.43: Loci of the return flow jet centreline trajectory, the jet half-width (δ_1), the jet width (δ_2) and the water surface in the global Cartesian coordinate system.	164
Figure 5.44: Variation of δ_1 with s over the full jet trajectory.	165
Figure 5.45: Variation of δ_1/b_o with ξ over (a) the full jet trajectory and over (b-d) the sections upstream of the baffle, between the baffle and the point of impingement and downstream of the point of impingement, respectively.	166
Figure 5.46: Variation of the C_2 coefficients for both δ_{1-} and δ_{1+} along the full jet centreline trajectory.	168
Figure 5.47: Variation of (a) δ_1 with s and of (b) δ_1/b_o with ξ along the full return flow jet trajectory.	169
Figure 5.48: Variation of δ_2 with s over the full jet trajectory.	170

Figure 5.49: Variation of δ_z/b_o with ξ over (a) the full jet trajectory and over (b-d) the sections upstream of the baffle, between the baffle and the point of impingement and downstream of the point of impingement, respectively.	171
Figure 5.50: Variation of (a) δ_z with s and of (b) δ_z/b_o with ξ along the full return flow jet trajectory.	173
Figure 5.51: (a) Dimensional and (b) nondimensional u mean velocities for wall jet-like (WJL) profiles.	174
Figure 5.52: Comparison of theoretical curves describing the variation of u/U_m with η for wall jet-like (WJL) profiles using (a) classical wall jet and (b) free mixing region definitions.	175
Figure 5.53: (a) Dimensional and (b) nondimensional v mean velocities for wall jet-like (WJL) profiles.	176
Figure 5.54: (a) Dimensional and (b) nondimensional mean Reynolds stress per unit mass (τ/ρ) for wall jet-like (WJL) profiles.	177
Figure 5.55: (a) Dimensional and (b) nondimensional mean kinetic energy per unit mass (KE) for wall jet-like (WJL) profiles.	178
Figure 5.56: (a) Dimensional and (b) nondimensional mean turbulent kinetic energy per unit mass (k) for wall jet-like (WJL) profiles.	179
Figure 5.57: Mean dissipation per unit mass (d) for wall jet-like (WJL) profiles.	180
Figure 5.58: Mean (a) vorticity (ω) and (b) strain (ϵ) for wall jet-like (WJL) profiles.	181
Figure 5.59: Mean Kolmogorov (a) length scales (l_k) and (b) velocity scales (v_k) for wall jet-like (WJL) profiles.	182
Figure 5.60: (a) Dimensional and (b) nondimensional u mean velocities for plane jet-like (PJL) profiles.	183
Figure 5.61: Variation of u/U_m with η for plane jet-like (PJL) profiles with equation [2.9] plotted for reference.	184
Figure 5.62: (a) Dimensional and (b) nondimensional v mean velocities for plane jet-like (PJL) profiles.	185
Figure 5.63: (a) Dimensional and (b) nondimensional mean Reynolds stress per unit mass (τ/ρ) for plane jet-like (PJL) profiles.	186
Figure 5.64: (a) Dimensional and (b) nondimensional mean kinetic energy per unit mass (KE) for plane jet-like (PJL) profiles.	187
Figure 5.65: (a) Dimensional and (b) nondimensional mean turbulent kinetic energy per unit mass (k) for plane jet-like (PJL) profiles.	188
Figure 5.66: Mean dissipation per unit mass (d) for plane jet-like (PJL) profiles.	189

Figure 5.67: Mean (a) vorticity (ω) and (b) strain (ϵ) for plane jet-like (PJL) profiles.....	190
Figure 5.68: Mean Kolmogorov (a) length scales (l_k) and (b) velocity scales (v_k) for plane jet-like (PJL) profiles.	191
Figure 5.69: (a) Dimensional and (b) nondimensional u mean velocities for surface jet-like (SJL) profiles.....	192
Figure 5.70: Variation of u/U_m with η for surface jet-like (SJL) profiles with equation [2.9] plotted for reference.	193
Figure 5.71: (a) Dimensional and (b) nondimensional v mean velocities for surface jet-like (SJL) profiles.....	194
Figure 5.72: (a) Dimensional and (b) nondimensional mean Reynolds stress per unit mass (τ/ρ) for surface jet-like (SJL) profiles.	195
Figure 5.73: (a) Dimensional and (b) nondimensional mean kinetic energy per unit mass (KE) for surface jet-like (SJL) profiles.....	196
Figure 5.74: Mean (a) turbulent kinetic energy per unit mass (k) and (b) dissipation per unit mass (d) for surface jet-like (SJL) profiles.	197
Figure 5.75: Mean (a) vorticity (ω) and (b) strain (ϵ) for surface jet-like (SJL) profiles.....	198
Figure 5.76: Mean Kolmogorov (a) length scales (l_k) and (b) velocity scales (v_k) for surface jet-like (SJL) profiles.....	199
Figure 5.77: (a) Dimensional and (b) nondimensional u mean velocities for return surface jet-like (SJL) profiles.....	200
Figure 5.78: Variation of u/U_m with η for return surface jet-like (SJL) profiles with equation [2.9] plotted for reference.	201
Figure 5.79: (a) Dimensional and (b) nondimensional u mean velocities for the first transition zone (TZ1) profiles.	202
Figure 5.80: (a) Dimensional and (b) nondimensional u mean velocities for the second transition zone (TZ2) profiles.	203
Figure 5.81: (a) Dimensional and (b) nondimensional u mean velocities for the return flow second transition zone (TZ2) profiles.	204
Figure 5.82: Variation of q with s over (a) the full jet trajectory and over (b-d) the sections upstream of the baffle, between the baffle and the point of impingement and downstream of the point of impingement, respectively.	205
Figure 5.83: Variation of (a) q/q_0 with ξ and of (b) q/q_0 with $\xi^{0.5}$ along the full jet trajectory.	207
Figure 5.84: Variation of (a) q with s and of (b) q/q_0 with ξ along the full return flow jet trajectory.	208

Figure 5.85: Variation of (a) q with s and of (b) q/q_0 with ξ along the full trajectory for both the main flow and the return flow components of the jet.	209
Figure 5.86: Variation of m with s over (a) the full jet trajectory and over (b-d) the sections upstream of the baffle, between the baffle and the point of impingement and downstream of the point of impingement, respectively.	210
Figure 5.87: Variation of (a) m/m_0 with ξ and of (b) m/m_0 with $\xi^{0.5}$ along the full jet trajectory.	212
Figure 5.88: Variation of (a) m with s and of (b) m/m_0 with ξ along the full return flow jet trajectory.	213
Figure 5.89: Variation of (a) m with s and of (b) m/m_0 with ξ along the full trajectory for both the main flow and the return flow components of the jet.	214
Figure 5.90: Variation of (a) v_c with s and of (b) v_c/U_m with ξ along the full jet trajectory.	215
Figure 8.1: Sample instantaneous (a) raw and (b) corrected and interpolated pixel displacement vector fields for tessera 14.	225
Figure 8.2: Sample instantaneous (a) raw and (b) corrected and interpolated pixel displacement vector fields for tessera 1.	226
Figure 8.3: Sample instantaneous (a) raw and (b) corrected and interpolated pixel displacement vector fields for tessera 2.	227
Figure 8.4: Sample instantaneous (a) raw and (b) corrected and interpolated pixel displacement vector fields for tessera 3.	228
Figure 8.5: Sample instantaneous (a) raw and (b) corrected and interpolated pixel displacement vector fields for tessera 4.	229
Figure 8.6: Sample instantaneous (a) raw and (b) corrected and interpolated pixel displacement vector fields for tessera 5.	230
Figure 8.7: Sample instantaneous (a) raw and (b) corrected and interpolated pixel displacement vector fields for tessera 6.	231
Figure 8.8: Sample instantaneous (a) raw and (b) corrected and interpolated pixel displacement vector fields for tessera 7.	232
Figure 8.9: Sample instantaneous (a) raw and (b) corrected and interpolated pixel displacement vector fields for tessera 8.	233
Figure 8.10: Sample instantaneous (a) raw and (b) corrected and interpolated pixel displacement vector fields for tessera 9.	234
Figure 8.11: Sample instantaneous (a) raw and (b) corrected and interpolated pixel displacement vector fields for tessera 10.	235
Figure 8.12: Sample instantaneous (a) raw and (b) corrected and interpolated pixel displacement vector fields for tessera 11.	236

Figure 8.13: Sample instantaneous (a) raw and (b) corrected and interpolated pixel displacement vector fields for tessera 12.	237
Figure 8.14: Sample instantaneous (a) raw and (b) corrected and interpolated pixel displacement vector fields for tessera 13.	238
Figure 8.15: Mean velocity vector fields for (a) tessera 14 and (b) tessera 1; individual scale.	239
Figure 8.16: Mean velocity vector fields for (a) tessera 2 and (b) tessera 3; individual scale.	240
Figure 8.17: Mean velocity vector fields for (a) tessera 4 and (b) tessera 5; individual scale.	241
Figure 8.18: Mean velocity vector fields for (a) tessera 6 and (b) tessera 7; individual scale.	242
Figure 8.19: Mean velocity vector fields for (a) tessera 8 and (b) tessera 9; individual scale.	243
Figure 8.20: Mean velocity vector fields for (a) tessera 10 and (b) tessera 11; individual scale.	244
Figure 8.21: Mean velocity vector fields for (a) tessera 12 and (b) tessera 13; individual scale.	245
Figure 8.22: Tessera 14 component of assembled mean velocity vector field mosaic.	246
Figure 8.23: Tessera 1 component of assembled mean velocity vector field mosaic...	247
Figure 8.24: Tessera 2 component of assembled mean velocity vector field mosaic...	248
Figure 8.25: Tessera 3 component of assembled mean velocity vector field mosaic...	249
Figure 8.26: Tessera 4 component of assembled mean velocity vector field mosaic...	250
Figure 8.27: Tessera 5 component of assembled mean velocity vector field mosaic...	251
Figure 8.28: Tessera 6 component of assembled mean velocity vector field mosaic...	252
Figure 8.29: Tessera 7 component of assembled mean velocity vector field mosaic...	253
Figure 8.30: Tessera 8 component of assembled mean velocity vector field mosaic...	254
Figure 8.31: Tessera 9 component of assembled mean velocity vector field mosaic...	255
Figure 8.32: Tessera 10 component of assembled mean velocity vector field mosaic.	256
Figure 8.33: Tessera 11 component of assembled mean velocity vector field mosaic.	257
Figure 8.34: Tessera 12 component of assembled mean velocity vector field mosaic.	258
Figure 8.35: Tessera 13 component of assembled mean velocity vector field mosaic.	259
Figure 8.36: Peak locking error in tessera 1 raw pixel displacement data.....	260
Figure 8.37: Peak locking error in tessera 2 raw pixel displacement data.....	261
Figure 8.38: Peak locking error in tessera 3 raw pixel displacement data.....	262
Figure 8.39: Peak locking error in tessera 4 raw pixel displacement data.....	263

Figure 8.40: Peak locking error in tessera 5 raw pixel displacement data.....	264
Figure 8.41: Peak locking error in tessera 6 raw pixel displacement data.....	265
Figure 8.42: Peak locking error in tessera 7 raw pixel displacement data.....	266
Figure 8.43: Peak locking error in tessera 8 raw pixel displacement data.....	267
Figure 8.44: Peak locking error in tessera 9 raw pixel displacement data.....	268
Figure 8.45 Peak locking error in tessera 10 raw pixel displacement data.....	269
Figure 8.46: Peak locking error in tessera 11 raw pixel displacement data.....	270
Figure 8.47: Peak locking error in tessera 12 raw pixel displacement data.....	271
Figure 8.48: Peak locking error in tessera 13 raw pixel displacement data.....	272
Figure 8.49: Peak locking error in tessera 14 raw pixel displacement data.....	273
Figure 8.50: (a-n) The cumulative average, plotted over increasing periods of time and averaging larger batches of PIV data files, of the sum of all turbulent kinetic energy (k) measurements in a tessera, presented for (a) tessera 1 through (n) tessera 14; showing that a sufficient amount of data was collected at each tessera for representative mean turbulent flow characteristics to be calculated.....	274
Figure 8.51: (a) Dimensional and (b) nondimensional u mean velocities for return surface jet-like (SJL) profiles.....	279
Figure 8.52: (a) Dimensional and (b) nondimensional v mean velocities for return surface jet-like (SJL) profiles.....	280
Figure 8.53: (a) Dimensional and (b) nondimensional mean Reynolds stress per unit mass (τ/ρ) for return surface jet-like (SJL) profiles.....	281
Figure 8.54: (a) Dimensional and (b) nondimensional mean kinetic energy per unit mass (KE) for return surface jet-like (SJL) profiles.	282
Figure 8.55: Mean (a) turbulent kinetic energy per unit mass (k) and (b) dissipation per unit mass (d) for return surface jet-like (SJL) profiles.....	283
Figure 8.56: Mean (a) vorticity (ω) and (b) strain (ϵ) for return surface jet-like (SJL) profiles.	284
Figure 8.57: Mean Kolmogorov (a) length scales (l_k) and (b) velocity scales (v_k) for return surface jet-like (SJL) profiles.	285
Figure 8.58: (a) Dimensional and (b) nondimensional u mean velocities for the first transition zone (TZ1) profiles.	286
Figure 8.59: (a) Dimensional and (b) nondimensional v mean velocities for the first transition zone (TZ1) profiles.	287
Figure 8.60: (a) Dimensional and (b) nondimensional mean Reynolds stress per unit mass (τ/ρ) for the first transition zone (TZ1) profiles.	288

Figure 8.61: (a) Dimensional and (b) nondimensional mean kinetic energy per unit mass (KE) for the first transition zone (TZ1) profiles.....	289
Figure 8.62: Mean (a) turbulent kinetic energy per unit mass (k) and (b) dissipation per unit mass (d) for the first transition zone (TZ1) profiles.	290
Figure 8.63: Mean (a) vorticity (ω) and (b) strain (ϵ) for the first transition zone (TZ1) profiles.....	291
Figure 8.64: Mean Kolmogorov (a) length scales (l_k) and (b) velocity scales (v_k) for the first transition zone (TZ1) profiles.....	292
Figure 8.65: (a) Dimensional and (b) nondimensional u mean velocities for the second transition zone (TZ2) profiles.	293
Figure 8.66: (a) Dimensional and (b) nondimensional v mean velocities for the second transition zone (TZ2) profiles.	294
Figure 8.67: (a) Dimensional and (b) nondimensional mean Reynolds stress per unit mass (τ/ρ) for the second transition zone (TZ2) profiles.	295
Figure 8.68: (a) Dimensional and (b) nondimensional mean kinetic energy per unit mass (KE) for the second transition zone (TZ2) profiles.....	296
Figure 8.69: Mean (a) turbulent kinetic energy per unit mass (k) and (b) dissipation per unit mass (d) for the second transition zone (TZ2) profiles.	297
Figure 8.70: Mean (a) vorticity (ω) and (b) strain (ϵ) for the second transition zone (TZ2) profiles.....	298
Figure 8.71: Mean Kolmogorov (a) length scales (l_k) and (b) velocity scales (v_k) for the second transition zone (TZ2) profiles.....	299
Figure 8.72: (a) Dimensional and (b) nondimensional u mean velocities for the return flow second transition zone (TZ2) profiles.	300
Figure 8.73: (a) Dimensional and (b) nondimensional v mean velocities for the return flow second transition zone (TZ2) profiles.	301
Figure 8.74: (a) Dimensional and (b) nondimensional mean Reynolds stress per unit mass (τ/ρ) for the return flow second transition zone (TZ2) profiles.....	302
Figure 8.75: (a) Dimensional and (b) nondimensional mean kinetic energy per unit mass (KE) for the return flow second transition zone (TZ2) profiles.....	303
Figure 8.76: Mean (a) turbulent kinetic energy per unit mass (k) and (b) dissipation per unit mass (d) for the return flow second transition zone (TZ2) profiles.....	304
Figure 8.77: Mean (a) vorticity (ω) and (b) strain (ϵ) for the return flow second transition zone (TZ2) profiles.....	305
Figure 8.78: Mean Kolmogorov (a) length scales (l_k) and (b) velocity scales (v_k) for the return flow second transition zone (TZ2) profiles.	306

Nomenclature

A	solid body rotation eddy area
b_o	slot width at gate
d	mean dissipation rate per unit mass
d_{px}	PIV pixel displacement vector
d_{pxx}	x-component PIV pixel displacement
d_{pxy}	y-component PIV pixel displacement
d_{pxz}	z-component pixel displacement (out-of-plane displacement)
e_u	error in x- or y-component velocity
e_v	error in total velocity
e_ω	error in vorticity
F	Froude number, $F = U_o / \sqrt{gb_o}$
g	acceleration due to gravity
h	baffle height
I_{plu}	peak locking intensity of d_{pxx}
I_{plv}	peak locking intensity of d_{pxy}
k	mean turbulent kinetic energy per unit mass
k_i	instantaneous turbulent kinetic energy per unit mass
KE	mean kinetic energy per unit mass
KE_i	instantaneous kinetic energy per unit mass
l_k	mean Kolmogorov length scale
m	mean momentum flux per unit mass, $m = \int_{n=\delta_{2-}}^{n=\delta_{2+}} u^2 dn$
m_o	mean momentum flux per unit mass at gate
M_o	momentum flux at the outlet for a plane turbulent jet, $M_o = 2\rho b_o U_o^2$
n	sectional coordinate normal to θ_c measured from local jet centreline in the outbound direction
p	mean pressure
p_i	instantaneous pressure
q	mean discharge intensity, $q = \int_{n=\delta_{2-}}^{n=\delta_{2+}} u dn$
q_e	entrainment intensity
q_o	discharge intensity at gate
Q_o	mean discharge at gate
r	solid body rotation eddy radius
R	Reynolds number, $R = b_o U_o / \nu$

s	axial coordinate along jet centreline trajectory measured from slot
S_{FOV}	image scale
t	time
t_k	mean Kolmogorov time scale
u_i	instantaneous x- and s-component velocities
u	mean x- and s-component velocities
u'	turbulent x- and s-component velocities
U_o	mean jet exit velocity
U_m	maximum mean axial velocity at jet section
v_i	instantaneous y- and n-component velocities
v	mean y- and n-component velocities
v'	turbulent y- and n-component velocities
v_e	mean entrainment velocity component
v_k	mean Kolmogorov velocity scale
V	voltage
$V_{i \max}$	maximum instantaneous velocity magnitude
V_{\max}	maximum mean velocity magnitude
V_{\min}	minimum mean velocity magnitude
w_i	instantaneous z-component velocity
w	mean z-component velocity
w'	turbulent z-component velocity
x	global Cartesian longitudinal coordinate measured from gate
x_o	longitudinal position of the baffle, measured from gate
y	global Cartesian normal coordinate measured from bed
y_1	depth upstream of gate in head tank
y_2	depth immediately downstream of gate
y_t	tailwater depth
z	global Cartesian orthogonal to x and y
α_e	entrainment coefficient
δ_{1+}	jet half-width along positive section n-stem, where $u = 0.5 U_m$
δ_{1-}	jet half-width along negative section n-stem, where $u = 0.5 U_m$
δ_{2+}	distance from local jet centreline to jet boundary along positive section n-stem, where $u = 0$

δ_{2-}	distance from local jet centreline to jet boundary along negative section n-stem, where $u = 0$
Δt	time separation
ΔH	driving head of the jet, $\Delta H = y_1 - y_2$
ϵ	mean strain
ϵ_i	instantaneous strain
γ	specific weight of water
Γ	mean circulation, $\Gamma = \int \omega dA$
η	nondimensional jet section ordinate, $\eta = n/\delta_1$
μ	viscosity of water
ν	kinematic viscosity of water, $\nu = \mu/\rho$
ξ	nondimensional jet centreline trajectory ordinate, $\xi = s/b_0$
ω	mean vorticity in the x-y plane, counter-clockwise considered positive
ω_i	instantaneous vorticity in the x-y plane, counter-clockwise considered positive
θ	displacement or velocity vector angle
θ_c	angle of mean velocity vector at jet centreline
ρ	mass density of water
σ_{pxx}	standard deviation of d_{pxx}
σ_{pxy}	standard deviation of d_{pxy}
τ	mean Reynolds shear stress, $\tau = \tau_{xy} = -\rho \overline{u'v'}$
τ_i	instantaneous Reynolds shear stress
τ_o	wall shear stress

1 Introduction

The topic of this current work is motivated by the study of Wu and Rajaratnam (1995a) on the effect of baffles on submerged flows. Therein, the authors conceptualize the submerged hydraulic jump as an energy dissipator and describe the limitations encountered when tailwater depths are larger than subcritical sequent depths in such flows. It is suggested that the employment of submerged jet flows as energy dissipators is generally avoided in civil engineering practice; attributed to the concern that high-velocity streams may continue for relatively large distances along a riverbed without appreciable dissipation and thereby cause serious downstream erosion. This erosion can damage native fish and wildlife river ecosystems as well as endanger the foundations of hydraulic structures and adjacent public works.

It is also suggested that the provision of baffle walls in these types of submerged flows may attenuate the risk of bed degradation and erosion. Introduced by Wu and Rajaratnam is the instance of the deflected wall jet, the flow structure in which a baffle wall is employed to deflect a plane wall jet in such a way that it travels upward as a plane turbulent jet to eventually become a plane surface jet at the free surface. Wu and Rajaratnam propose that such a deflected wall jet can dissipate energy similarly to a deeply submerged hydraulic jumps without the associated erosion risks under certain conditions. A video still obtained from a dye visualization test of the plane deflected wall jet is shown in Figure 1.1. It is this flow that is presently studied.

The velocity and pressure data assembled by Wu and Rajaratnam is time averaged in nature and was collected using standard Prandtl tube point measurement techniques. Although a wealth of information concerning both the mean flow structure and velocity similarity configurations are presented by the authors, there currently exists no detailed mean or turbulent data set describing the whole flow field of the deflected wall jet.

This study aims to remedy the deficiency by employing the particle image velocimetry (PIV) technique in a limited experimental investigation of the phenomenon. The specific PIV arrangement is quite non-standard. It divides a large flow field into individual tesserae, which are imaged and processed separately. The resulting data sets are then assembled into a final mosaic fully describing the experimental area of interest, providing greater spatial and velocity resolution than could be achieved by studying the mosaic as a whole. The measurement programme and analyses presented in the current work provide original instantaneous, mean and turbulent data including but not limited to: velocity, Reynolds stress, vorticity and turbulent kinetic energy.

The structure of this thesis follows the progression of the theoretical investigation, the experimental programme and the analysis of resultant data. A detailed literature review is found in §2 that considers the theory of plane turbulent jets. It focuses, in particular, on the classic plane jet, but considers also the plane jet in a crossflow, the plane wall jet and the plane surface jet, as these are the constitutive elements of the

deflected plane wall jet, as outlined by Wu and Rajaratnam (1995a). The experimental methods of the investigation are outlined in §3. This includes a brief outline of PIV methodology and follows with a description of the flume arrangement, the PIV instrumentation setup and the measurement programme. Details of the primary PIV processing and supplementary computations are presented in §4, along with sources of error. Analysis of the resultant data is presented in §5, as well as concurrent discussions regarding the findings of this research and its relationship to the current state of knowledge on the subject. Conclusions and recommendations for future work are given in §6. References are provided in §7 and the appendix is §8.

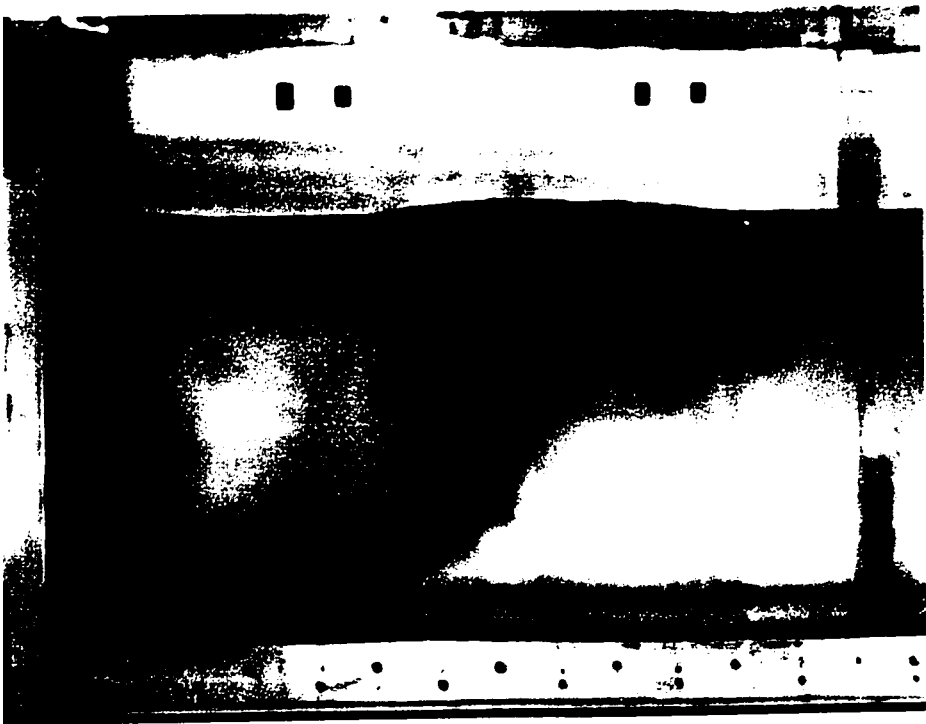


Figure 1.1: Dye visualization still of the plane deflected wall jet.

2 Literature Review

Because the plane turbulent deflected wall jet has plane jet-like, wall jet-like and surface jet-like constitutive elements, condensed reviews of the current states of knowledge on these subjects are presented below. More consideration will be given to the plane jet as the other cases may be considered as special cases of the plane jet, and analyses are similar. An excellent review of jet theory, and especially that of a plane and wall jets, is presented by Rajaratnam in the book *Turbulent Jets* (1976), and it is from this volume that a great portion of the following discussion is derived.

2.1 Plane Turbulent Jets

2.1.1 Classic Plane Jet

The classic plane turbulent jet (also called simply the plane jet) can be considered as a jet of either water or air issuing from a plane nozzle into a large body of an identical fluid, with the slot width at the upstream gate defined as $2b_0$, the mean jet exit velocity defined as U_0 and the mean jet discharge defined as Q_0 . In such a configuration, the origin of the Cartesian coordinate system is located at the centreline of the issuing jet and at the downstream edge of the slot, with x being the coordinate measured from the gate in the direction of the jet axis, y being the coordinate measured normal to x in the direction of the plane surface and z being the third axis of the coordinate system orthogonal to the others. The two-dimensionality of the plane jet results in a plane of symmetry coincident with the x - z plane and hence normal to the slot at the upstream gate. Figure 2.1 shows the definition sketch of this type of plane turbulent jet.

The fluid discharged from the gate opening may be assumed to be of relatively constant mean velocity, with a pronounced velocity discontinuity between the jet and the surrounding fluid both above and below the body of the jet (Albertson *et al.* 1950). The eddies generated in this region of high shear will immediately result in a lateral mixing process whereby the kinetic energy of the oncoming flow is steadily converted into turbulence, with the latter steadily decaying through viscous shear. Due to the turbulent nature of the mixing region, the fluid within the jet undergoes both lateral diffusion and deceleration, with fluid from the surrounding area being brought into motion or entrained into the body of the jet. Thus the deceleration of the fluid in the jet is accompanied by a simultaneous acceleration of the surrounding fluid, resulting in both an increase in jet width and discharge intensity (q) at successive sections of the jet with distance from the efflux section and origin.

The mean flow of the plane jet can be divided into two distinct regions of developmental stability: the developing flow region and the fully developed flow region. In the first region, nearest to the efflux section, the jet begins with a near-uniform velocity distribution of $u = U_0$. Turbulence generated by each of the shear layers bounding the plane jet penetrate both outwards and inwards, both away from and toward the plane of symmetry of the jet. A wedge-like region of undiminished mean velocity equal to U_0 can be found between the successively closer turbulent

fronts propagating towards the plane of symmetry, as shown in Figure 2.2. This zone is called the potential core and has a length of approximately $12b_0$ measured from the origin (Rajaratnam 1976). Its presence defines the developing flow region; that is, the limit of this zone of flow establishment is reached when the mixing region has penetrated to the centreline of the jet and there is no longer any province where U_0 exists unchanged.

The second region, is characterized by the lack of a potential core and by the establishment of dynamic similarity whereby the diffusion process and the growth of the jet continue without essential change in character. In this fully developed flow region, further entrainment of the surrounding fluid by the expanding eddy region is balanced inertially by a continuous reduction in the velocity of the entire body region (Albertson *et al.* 1950) of the jet. It is here that the most interesting relationships between the various parameters of the plane turbulent jet can be and historically have been identified and compared. In this region it is noted that at each section taken along the trajectory, the axial component velocity u decreases continuously from a maximum U_m at the jet centreline to a zero value with distance away from the central axis. Two points of interest are defined in such velocity profiles: the point at which the mean velocity is equal to half of the maximum velocity, where $u = 0.5 U_m$, and the point at which the velocity is equal to zero, where $u = 0$. The first location is defined as the jet half-width δ_1 and the second is defined as the jet width δ_2 .

The similarity of the u profiles at various longitudinal sections on the x -axis when the flow is completely established can best be observed when the profiles are non-dimensionalized and collapsed onto each other. The standard non-dimensionalizing quantities are called the velocity scale and the length scale, and are defined respectively as U_m and δ_1 . Plotting u/U_m against $\eta = y/\delta_1$ for different longitudinal sections yields velocity distributions that fall on one common geometric curve. They are thus said to be similar, exhibiting a strong relationship of the form $u/U_m = f(\eta)$.

In order to study the similar velocity distributions found in the fully developed region, it is advantageous to investigate the phenomenon from an analytical standpoint and develop the equations of motion for the plane turbulent jet. Following the procedure and logic outlined by Rajaratnam (1976), one accepts the decomposition of velocity and pressure terms into mean and fluctuating components and begins with the three dimensional Reynolds equations and the continuity equation for incompressible flow. Presuming the flow to be both steady and completely two dimensional, terms including time derivatives or w -component velocities and derivatives are dropped from the equations. Further reductions to the equations are made following the observation that u is generally much larger than v in a large portion of the jet and that both the velocity and pressure gradients are much smaller in the x -coordinate direction than the y -coordinate direction. After equation rearrangement, a final assumption of the pressure gradient in the axial direction being

negligibly small is made (assuming a simple hydrostatic pressure distribution), resulting in the well-known equations of motion for the plane jet:

$$u \frac{\partial u}{\partial x} + v \frac{\partial u}{\partial y} = \frac{1}{\rho} \frac{\partial \tau}{\partial y} \quad [2.1]$$

$$\frac{\partial u}{\partial x} + \frac{\partial v}{\partial y} = 0 \quad [2.2]$$

where u , v and w are the mean component velocities in the x -, y - and z -directions, respectively, and τ is the mean Reynolds shear stress.

Further theoretical analyses can be performed with the above equations in order to better understand the mean flow of the plane jet. Approaches have been developed in which the equations of motion are integrated across the jet and conservation integrals for momentum, energy and volume derived (Kotsovinos 1975). Rajaratnam derives the integral momentum equation by multiplying equation [2.1] by ρ and integrating across y . Employing our assumption on the nature of the velocity distribution at different jet sections and from considerations of symmetry, the remaining equation can be expressed as:

$$\frac{d}{dx} \int_0^\infty \rho u^2 dy = 0 \quad [2.3]$$

This equation indicates that the rate of change of momentum flux in the x -direction is zero and that therefore the momentum flux, $M_o = 2\rho b_o U_o^2$, should be conserved. The momentum flux is an important physical quantity controlling the behaviour of the plane jet. It effectively replaces the individual values of b_o and U_o in any similarity analysis and indicates that, for a given value of M_o , the same jet behaviour is obtained for different combinations of b_o and U_o (Rajaratnam 1976). A parallel analysis of the energy flux, performed by multiplying equation [2.1] by ρu and integrating over y yields the following equation, indicates that the rate of decrease of the kinetic energy flux is equal to the rate at which turbulence is produced, supporting the assertion that the mixing action of the jet converts kinetic energy into turbulence which is ultimately dissipated:

$$\frac{d}{dx} \int_0^\infty \frac{\rho u^2}{2} dy = - \int_0^\infty \tau \frac{\partial u}{\partial y} dy \quad [2.4]$$

Rajaratnam (1976) also derives the volume flux integral equation and discusses the entrainment hypothesis originally introduced by Morton *et al.* (1956) relating to the plane turbulent jet. Here, the discharge intensity at any section of the jet is defined as twice the integral of u from $y = 0$ to $y = \infty$ and the rate of change of q with longitudinal distance from the gate can be obtained from integration of equation [2.2] and finally written as:

$$\frac{dq}{dx} = \frac{d}{dx} \int_{-\infty}^{\infty} u dy = -v_e \quad [2.5]$$

where v_e is the entrainment velocity magnitude component, representing the velocity magnitude of the fluid being brought into the jet. The entrainment velocity could also be expressed as $-v_e = \alpha_e U_m$, with α_e representing the entrainment coefficient. As explained earlier, the jet entrains a considerable amount of the surrounding fluid as it moves forward. If momentum is considered to be conserved, it would follow that there should be no axial component to the entrainment velocity, however, Heskestad (1965) has reported that the flow near the edge of the jet enters the jet at angles in excess of normal to the x-axis. This indicates that momentum is not actually conserved and that the assumptions used in the determination of equation [2.3] are imperfect. Kotsovinos (1978) notes a loss of $0.2M_0$ in the momentum flux of a plane jet approximately $100b_0$ downstream of the origin and presents an equation describing the variation.

Regardless, from dimensional considerations of the three flux integrals and the Reynolds and continuity equations it is possible to present general proportionalities describing the decay of the maximum mean centreline velocity, the jet growth rate, and the increase of the jet discharge intensity in the context of the velocity distribution relationship $u/U_m = f(\eta)$ noted earlier. Substitution and rearrangement suggest that $U_m \propto 1/\sqrt{x}$, that $\delta_1 \propto x$ and that $v_e \propto U_m$. Further dimensional analysis (Rajaratnam 1976) produces the following three semi-empirical equations with the coefficients C_1 , C_2 and C_3 requiring evaluation with experimental data:

$$\frac{U_m}{U_0} = \frac{C_1}{\sqrt{x/b_0}} \quad [2.6]$$

$$\delta_1/b_0 = C_2 (x/b_0) \quad [2.7]$$

$$q/q_0 = C_3 \sqrt{x/b_0} \quad [2.8]$$

There exists a long history of experimental and mathematical studies performed to give explanation and prediction to the velocity distribution in the plane turbulent jet. Tollmien (1926) and Görtler (1942) each produced theoretical approximations to the similarity curve by substituting varying hypothetical relations between shear stress and velocity gradients based on the equations of Prandtl (concepts such as mixing length and eddy viscosity) in the simplified equations of motion. Förthmann (1934) and Reichardt (1941) both collected extensive data sets of mean flow properties that adequately validated the previous semi-empirical solutions. Reichardt derived a solution similar to those of Tollmien and Görtler by instead using a thermal conduction analogy as the shear stress substitution in the equations of motion while Zijnen (1958) showed that the velocity distribution could be satisfactorily represented by a Gaussian curve. Corrsin (1943) noted certain shortcomings of the hypotheses used by Tollmien and Görtler (reported by Albertson *et al.* 1950 and by Miller and Comings 1957) and confirmed the insensitivity of their velocity functions to their

employed closure relationships when he conducted detailed measurements of the turbulence within two dimensional jets. Additional detailed mean and turbulent data was collected by Albertson *et al.* (1950), Miller and Comings (1957), Zijnen (1958), Heskestad (1965) and Goldshmidt and Eskinazi (1966) and supplementary solutions were presented by them.

The resulting wealth of theoretical arguments, experimental data and semi-empirical solutions have lead to a refined set of functions which describe most of the experimenta data accurately. It can be noted that Tollmein's solution appears to provide a better fit in the outer region of the velocity profile while Görtler's solution appears superior near the jet axis. The following solution of Reichardt provides a good general fit (Goldshmidt and Eskinazi 1966) and is considered a suitable $f(\eta)$ approximation:

$$u/U_m = e^{-0.693\eta^2} \quad [2.9]$$

Rajaratnam (1976) reports that due to the imprecise methods of locating the virtual origin of plane jets, it can be taken as coincident with the origin described earlier. In fact, most of the solutions historically presented can be reworked in forms of equations [2.6], [2.7] and [2.8] and coefficients compared. The following are accepted coefficient values: $C_1 = 3.50$, $C_2 = 0.1$ and $C_3 = 0.44$, with $\alpha_c = 0.053$ obtained from equation [2.5], as reported by Rajaratnam. They result in the following formulae:

$$\frac{U_m}{U_o} = \frac{3.50}{\sqrt{x/b_o}} \quad [2.10]$$

$$\delta_1 = 0.1x \quad [2.11]$$

$$q/q_o = 0.44\sqrt{x/b_o} \quad [2.12]$$

$$v_c = -0.053U_m \quad [2.13]$$

2.1.2 Plane Jet in a Crossflow

Consider a plane turbulent jet issuing into a body of fluid which has a uniform velocity, and orient the jet and slot so that the jet exit velocity is normal to the uniform velocity. This flow is shown in Figure 2.3 and describes the case of a plane turbulent jet in a crossflow. The initial characteristics of the such a jet are identical to those of the plane jet: the slot width is defined as $2b_o$, the mean jet exit velocity as U_o and the mean jet discharge as Q_o . The origin of the global Cartesian coordinate system is located at the centreline of the jet at efflux section, with x measured from and normal to the gate, y measured normal to x and in the direction of flow in the surrounding fluid body, and z orthogonal to both the x - and y -coordinate axes. There is, however, no plane of symmetry. The trajectory of the jet centreline is curved in nature and therefore not coincident with the x -axis; it defines the local coordinate system through which the plane jet in a crossflow can be studied and is defined by the locus along which the maximum mean axial jet velocity U_m exists. This frame of reference shares

its origin with the global frame, but considers the s -coordinate axis (defined by the trajectory), θ_c (defined as the angle between U_m and the x -axis) and the n -coordinate axis (defined as normal to θ_c in the outbound direction) as seen in the provided figure.

For reasons which will be obvious in §2.4, it becomes convenient to neglect a detailed fluid mechanical analysis of the plane jet in a crossflow. The significant observation taken from the current literature is that there exists a similarity in velocity profiles taken at different sections along the s -axis in the developed flow region that can be approached in a manner comparable to that in §2.1 and that growth rate of the jet is non-symmetrical (Yu-Leuk and Wood 1966). As such, let δ_{1+} and δ_{2+} define the jet half-width and jet width along the positive (outbound) section n -stem, where $u = 0.5U_m$ and $u = 0$ respectively, and let δ_{1-} and δ_{2-} define the same values along the negative (inbound) section n -stem. Likewise, the dual length scales are defined as δ_{1+} and δ_{2+} with the velocity scale as U_m .

2.2 Plane Turbulent Wall Jets

The classic plane turbulent wall jet (also called simply the wall jet) can be considered as a jet of either water or air issuing from a plane nozzle tangentially onto a flat plate or bed that is submerged in a semi-infinite body of an identical fluid. The slot width at the upstream gate is defined as b_o , the mean jet exit velocity defined as U_o and the mean jet discharge defined as Q_o , much like the definitions applied to a plane jet. In such a configuration, the origin of the Cartesian coordinate system framing the flow is located on the bed and at the downstream edge of the slot. The x -coordinate is measured from the gate in the direction of the jet axis, with the y -axis taken normal to the x -axis towards the free surface and with the z -axis of the coordinate system orthogonal to both the x - and y -coordinate axes. Figure 2.4 shows the definition sketch of plane turbulent wall jet.

The behaviour of the fluid and the mean characteristics of the jet as it exits the outlet closely resemble those of the plane jet. In both cases a shear layer is formed where the velocity discontinuity exists, there is the presence of a potential core and therefore there is both a developing and a fully developed flow region to the body of the jet. The surrounding fluid is likewise also entrained into the mixing region of the wall jet. Like the plane jet, the length of the developing region of a plane wall jet is also equal to approximately $12b_o$, as measured from the coordinate system origin (Rajaratnam 1965a). However, unlike the former, this flow is not symmetrical about the x - z plane, nor can its virtual origin be considered coincident with the coordinate system origin. It is, in fact, located approximately $10b_o$ upstream of the global origin (Rajaratnam 1976). The reason for the differences is obvious: the presence of the bed. Instead of two shear layers propagating both toward and away from each other in an axisymmetrical manner, there is a growing free-mixing region on one side and a boundary layer of thickness δ on the other.

Overlooking the boundary layer and the slightly different mechanisms by which the potential core of the plane turbulent wall jet is consumed, the wall jet presents itself surprisingly similar to the upper half of the plane turbulent jet. It is defined with via a corresponding logic. In the fully developed flow region, it is noted that at each section taken along the trajectory, the axial component velocity u decreases continuously from a maximum U_m where $y = \delta$ to a zero value some distance above the bed. The two main locations of interest in such velocity profiles are defined like those in the plane jet: the point at which the mean velocity is equal to half of the maximum velocity, where $u = 0.5 U_m$ with the caveat $\partial u / \partial y < 0$, and the point at which the velocity is equal to zero, where $u = 0$ with that same caveat. The first location is defined as the jet half-width δ_1 and the second is defined as the jet width δ_2 .

Similarity of the u profiles at various sections along the x -axis (when the flow is completely established) is observed when the profiles are non-dimensionalized and superposed. The velocity scale and length scales are taken as U_m and δ_1 , respectively. Plotting u / U_m against $\eta = y / \delta_1$ for different longitudinal sections yields a common similarity curve of the form $u / U_m = g(\eta)$.

Following closely the arguments presented in §2.1 and again neglecting the effects of any longitudinal pressure gradient, it can be shown that the simplified equations of motion for the plane turbulent wall jet are as follows:

$$u \frac{\partial u}{\partial x} + v \frac{\partial u}{\partial y} = v \frac{\partial^2 u}{\partial y^2} + \frac{1}{\rho} \frac{\partial \tau}{\partial y} \quad [2.14]$$

$$\frac{\partial u}{\partial x} + \frac{\partial v}{\partial y} = 0 \quad [2.15]$$

The momentum, energy and volume fluxes can be similarly produced, integrated and manipulated. This process introduces the wall shear stress τ_o as an important term, and it becomes clear that the friction at the wall is a decisive agency that must be given a prominent place in any theory of the turbulent plane wall jet (Glauert 1956). Coupled with the same type of dimensional analysis used in the analysis of the plane jet, the relationships $U_m \propto 1/\sqrt{x}$, that $\delta_1 \propto x$, $\tau_o \propto 1/x$ and $v_e \propto U_m$ are suggested Rajaratnam (1976). Theoretical arguments and experimental observations have been given by Förthmann (1934), Glauert (1956), Sigalla (1958), Schwartz and Cosart (1961), Myers *et al.* (1963), Verhoff (1963), Rajaratnam (1965a-c), Rajaratnam and Subramanya (1967 and 1968) and Wu and Rajaratnam (1995b). In his summary of the works completed previous to 1976, Rajaratnam reports the following formulae as describing the turbulent plane wall jet:

$$u / U_m = 1.48 \eta^{1/7} [1 - \text{erf}(0.68 \eta)] \quad [2.16]$$

$$\frac{U_m}{U_o} = \frac{3.50}{\sqrt{x/b_o}} \quad [2.17]$$

$$\delta_1 = 0.068x \quad [2.18]$$

$$q/q_0 = 0.248(x/b_0) \quad [2.19]$$

$$v_c = -0.035U_m \quad [2.20]$$

2.3 Plane Turbulent Surface Jets

A plane turbulent surface jet can be observed as a fluid jet of thickness b_0 issuing from a slot into a semi-infinite body or large channel of an identical stagnant fluid, where the jet enters tangentially to the free surface and the bed of the channel is at such a depth as to hold no influence over the behaviour of the jet. There exists a near-uniform mean velocity as the jet issues into the body of fluid defined as U_0 and a mean discharge defined as Q_0 . This describes the plane turbulent surface jet. In such a configuration, the origin of the Cartesian coordinate system framing the flow is located at the water surface and at the downstream edge of the slot. The x-coordinate axis is measured from the gate in the direction of the plane surface jet flow, with the y-coordinate axis taken normal to the x-axis toward the bed and with the z-coordinate axis orthogonal to both the x- and y-coordinate axes. Figure 2.5 shows the definition sketch of the plane turbulent surface jet.

If one were to mirror this two-dimensional flow about its x-axis, it would very closely resemble to upper half of the plane jet of §2.1 or the plane wall jet of §2.2. A number of parallels can be drawn from the previous reviews. On the underside of the surface jet a shear layer is formed due to the velocity discontinuity between the jet and the ambient into which it enters. Surrounding fluid is entrained into the body of the jet. There exists a potential core that is consumed when the mixing region of the shear layer eventually reaches the surface, as well as developing (approximately $12b_0$ in length measured from the origin) and fully developed flow regions. As is the case for the plane wall jet, the virtual origin of the plane turbulent surface jet is located approximately $10b_0$ behind the global Cartesian origin.

In the fully developed flow region, the axial component velocity u is at its maximum U_m very near to the water surface and smoothly decreases to zero at some distance below. Important characteristic locations and scales along velocity profiles taken at various sections on the x-axis are defined as those of the plane jet. The jet half-width δ_1 is defined where the mean velocity is equal to half of the maximum velocity and the jet width is defined where the velocity is equal to zero. Similarity of the u profiles at various sections along the x-axis is observed when u/U_m is plotted against $\eta = y/\delta_1$ for different longitudinal sections, with the mean velocity relationship expressed in the form $u/U_m = h(\eta)$. Rajaratnam and Humphries (1984) report that equation [2.9], $u/U_m = e^{-0.693\eta^2}$, adequately describes both their own data and that of Vanvari and Chu (1974) for $\eta < 1.4$. Following closely the arguments and assumptions presented in §2.1, it can be shown that the simplified equations of motion for the plane turbulent surface jet are equations [2.1] and [2.2] and that the relationships $U_m \propto 1/\sqrt{x}$, $\delta_1 \propto x$ and $v_c \propto U_m$ are valid through flux integral analysis

and dimensional considerations. The following equations describing the mean flow of the plane turbulent surface jet are reported by Rajaratnam and Humphries (1984):

$$\frac{U_m}{U_o} = \frac{3.10}{\sqrt{x/b_o}} \quad [2.21]$$

$$\delta_i = 0.09x \quad [2.22]$$

$$v_e = -0.037U_m \quad [2.23]$$

More recent studies, including those by Swean *et al.* (1989) and Ead and Rajaratnam (2001), provide additional experimental data of more jets with finite depths of tailwater and adverse pressure gradients, and analyses attacking the acknowledged decay of momentum flux in jets which entrain fluid.

2.4 Plane Turbulent Deflected Wall Jets

Consider a supercritical plane jet of water issuing into a rectangular channel filled with a identical fluid, where the jet nozzle is set tangentially to the flume bed and a baffle of height h is placed on the bed at a distance of x_o from the outlet. The baffle extends across the entire width of the channel and is oriented perpendicular to the channel side walls. The slot width at the upstream gate is defined as b_o and the mean jet exit velocity is defined as U_o . The jet discharge is defined as Q_o . Consider the origin of the coordinate system as located on the bed and at the downstream edge of the slot. The x -axis is measured from the gate in the downstream direction, the y -axis is taken normal to the x -axis towards the water surface and the z -axis is orthogonal to both x and y . The water level upstream of the gate is called y_1 and the level immediately downstream is called y_2 , with the tailwater called y_t . The driving head of the jet is expressed as $\Delta H = y_1 - y_2$.

The plane deflected wall jet is observed if the jet behaves like a plane wall jet upstream of the baffle, where it is deflected and travels upward, behaving as a curved plane turbulent jet, with a return flow between the inbound face of the jet and the gate, and eventually behaves like a plane surface jet at the water surface. This return flow is defined by the axial velocity profiles passing through zero at some sectional ordinate and having negative axial velocities past that ordinate, and occurs as a result of the effective jet confinement. It is similar to actual experimental data, such as in the submerged flow in a sluice way (Rajaratnam 1965a) or in the flow of a plane surface jet in shallow tailwater (Ead and Rajaratnam 2001). Figure 2.6 shows both the mean flow pattern of and the definition sketch for the plane turbulent wall jet.

It is mentioned in §1 that Wu and Rajaratnam (1995a) discuss the submerged hydraulic jump as an energy dissipator. The authors note that although submerged jumps are well understood phenomena, they are not commonly used in practice, for fear of serious bed erosion under sub-optimal tailwater level conditions. As an alternative, Wu and Rajaratnam employ a baffle wall in a configuration physically identical to the one described above, and study the effects of the baffle on the

submerged plane jet flow. Their experiments were performed in a flume 7.60 m long, 0.466 m wide and 0.60 m deep with varying baffle heights, baffle positions, tailwater levels, and Froude numbers. Wu and Rajaratnam measured time-averaged velocities and pressures using both pitch probes and Prandtl tubes connected to either transducers or manometer boards.

Their experiments identify two possible flow states: the first being that described earlier, of a plane turbulent deflected wall jet (defined by Wu and Rajaratnam as the deflected surface jet) having wall jet-like (WJL), plane jet-like (PJL) and surface jet-like (SJL) constitutive elements; and the second being that of a stable reattached wall jet, where the main flow passes over the baffle and reattaches to the bed of the flume. In the case of the deflected wall jet, three eddies are observed. They are positioned in relation to the centreline of the jet (defined by the locus of the maximum velocity filament) and the baffle. There first exists a large eddy of clockwise rotation on the outbound side of the curved jet extending to the downstream end of the flume. Second is an eddy of counter-clockwise rotation and significant circulation (Wu and Rajaratnam 1995a) bounded by the upstream flume gate and the jet centreline. There thirdly exists a small eddy of clockwise rotation upstream of the baffle and below the jet centreline, with a diameter of the same order as h . A reference curve was produced by plotting x_o/y_i against h/y_i which identifies the stable reattaching and stable deflected wall jet regimes as well as a transition region where the jet oscillates between the two stable patterns.

Further experiments were conducted by Wu and Rajaratnam on the deflected wall jet case with mean u and v velocity profiles taken at various stations along the length and height of the flow. Analysis was performed parallel to either wall jet or surface jet theory, with no distinction made when the jet is plane jet-like. In the main flow region before the baffle (wall jet-like) it was found that the velocity profiles are similar and well represented by the equations of §2.2. It is reported that the growth rate of the length scale δ_1 is not greatly affected by the presence of the baffle until the jet gets very close to the baffle and that the velocity scale U_m decays in the familiar manner. The curved plane jet-like region begins approximately at $x = x_o$ and it is here that deviation is noted: there is a rapid decrease in U_m that reaches a minimum near where the jet trajectory approaches the free surface and there is enhanced entrainment due to the curved nature of the jet in this region. In the main flow region downstream of the point where the jet centreline reaches the free surface (plane jet-like) Wu and Rajaratnam observe that velocity profiles are similar but somewhat different than given in §2.3. The length scale has a growth rate smaller than for the classic plane surface jet and is approximately $2b_o$ at the upstream limit of the region. Maximum velocity decay occurs as it would for a surface jet that is located upstream of the gate.

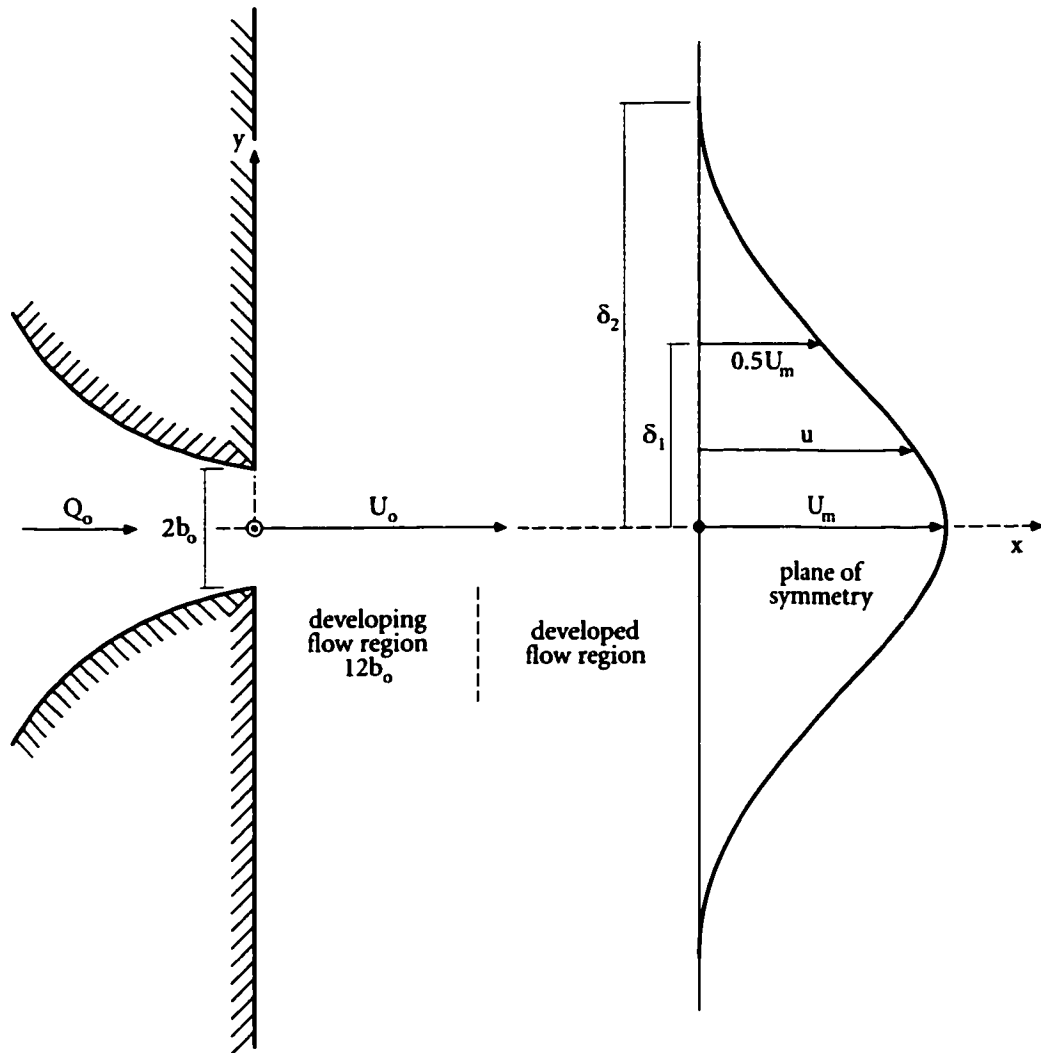


Figure 2.1: Plane turbulent jet definition sketch.

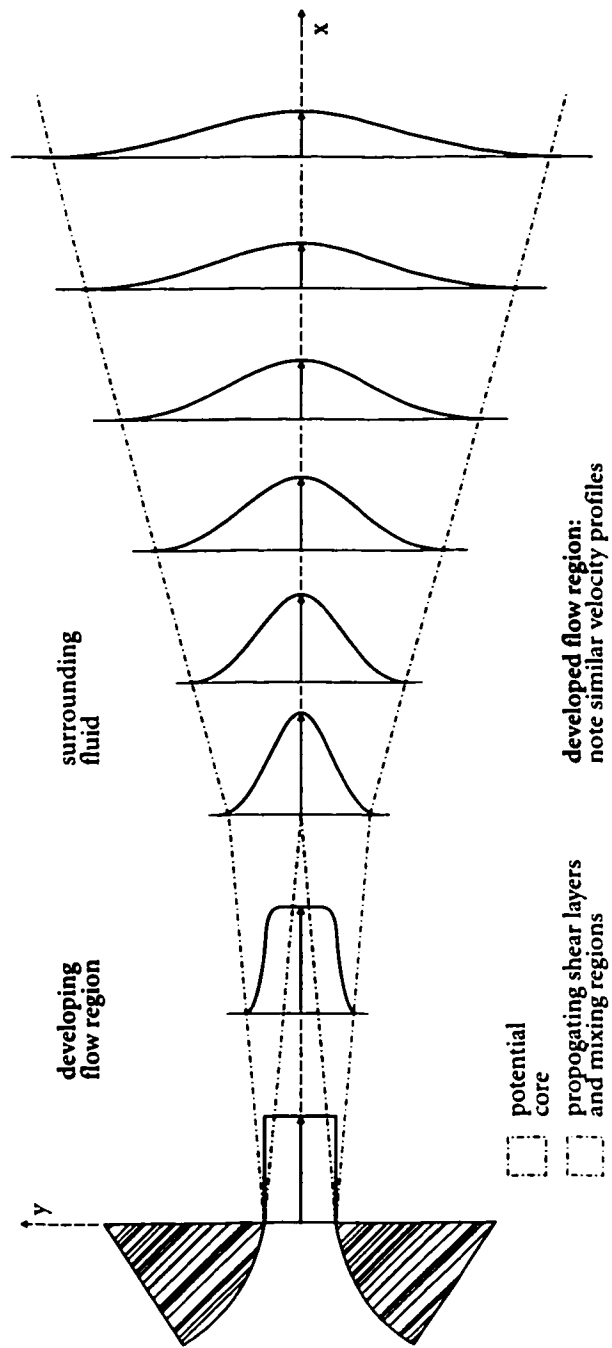


Figure 2.2: Plane turbulent jet potential core and development sketch.

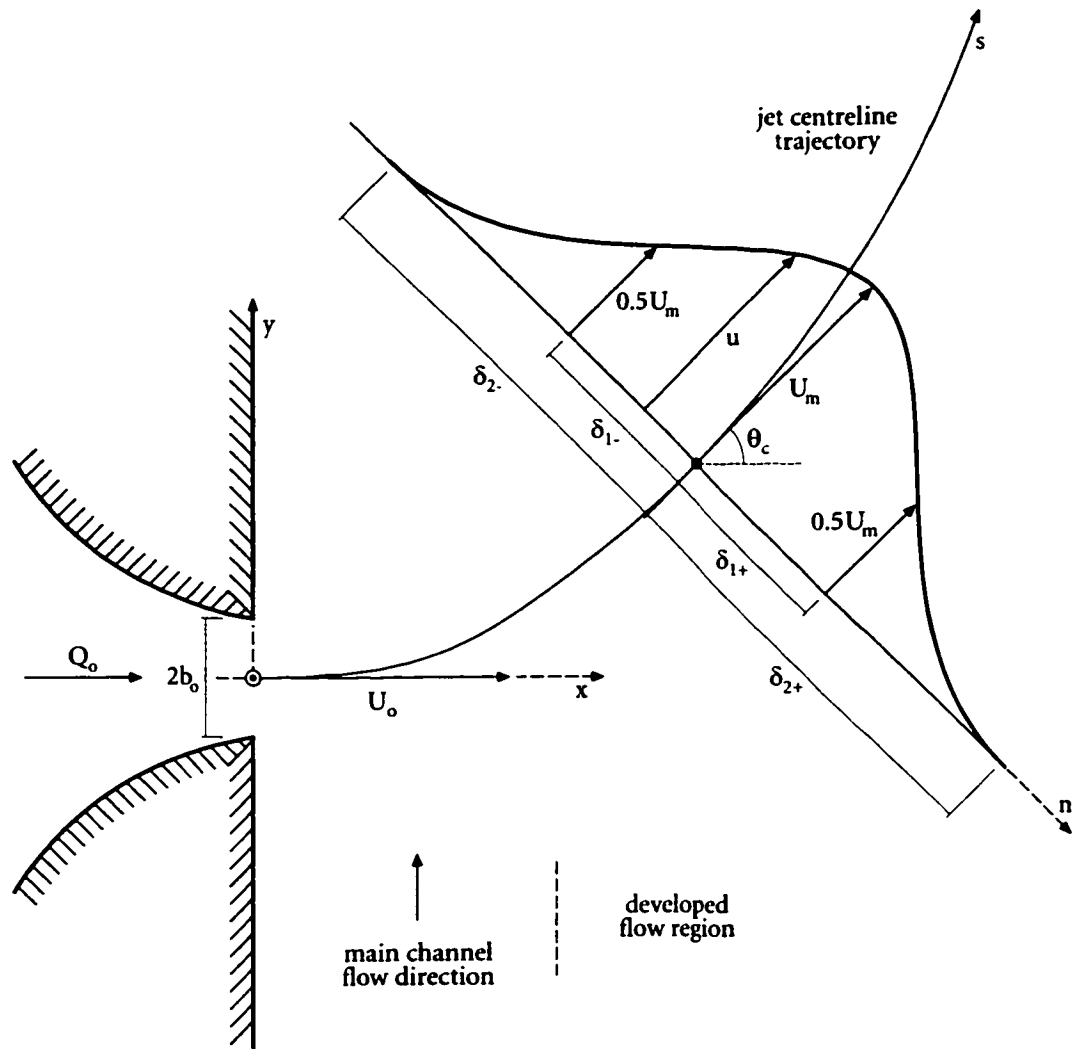


Figure 2.3: Plane turbulent jet in a crossflow definition sketch.

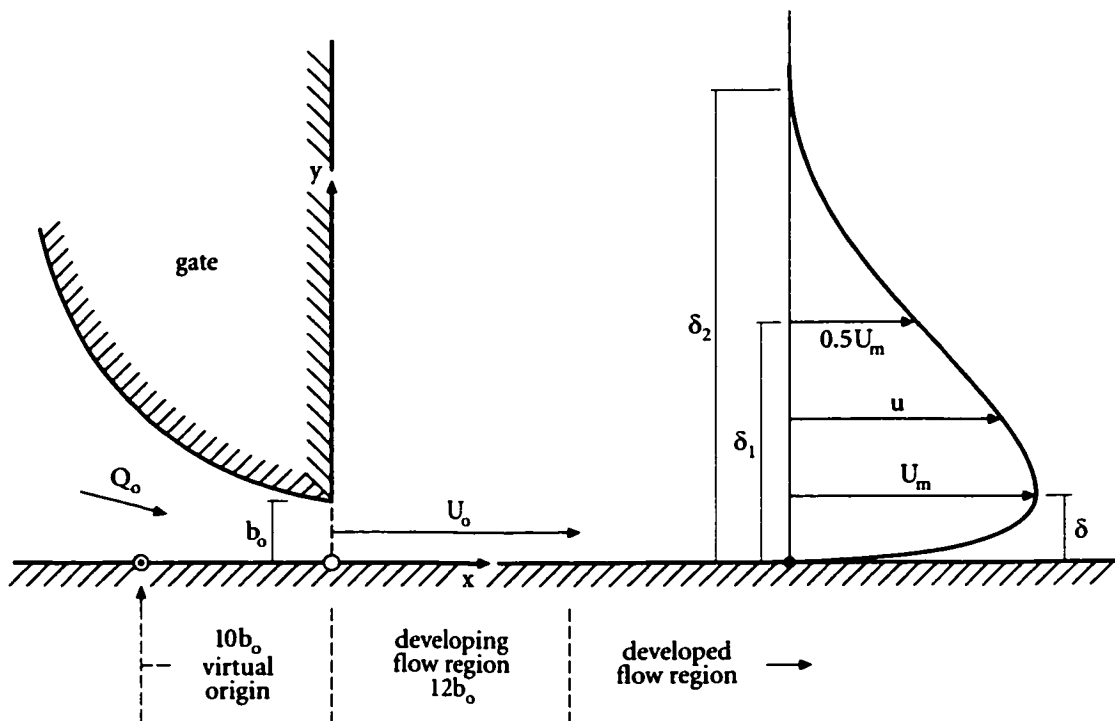


Figure 2.4: Plane turbulent wall jet definition sketch.

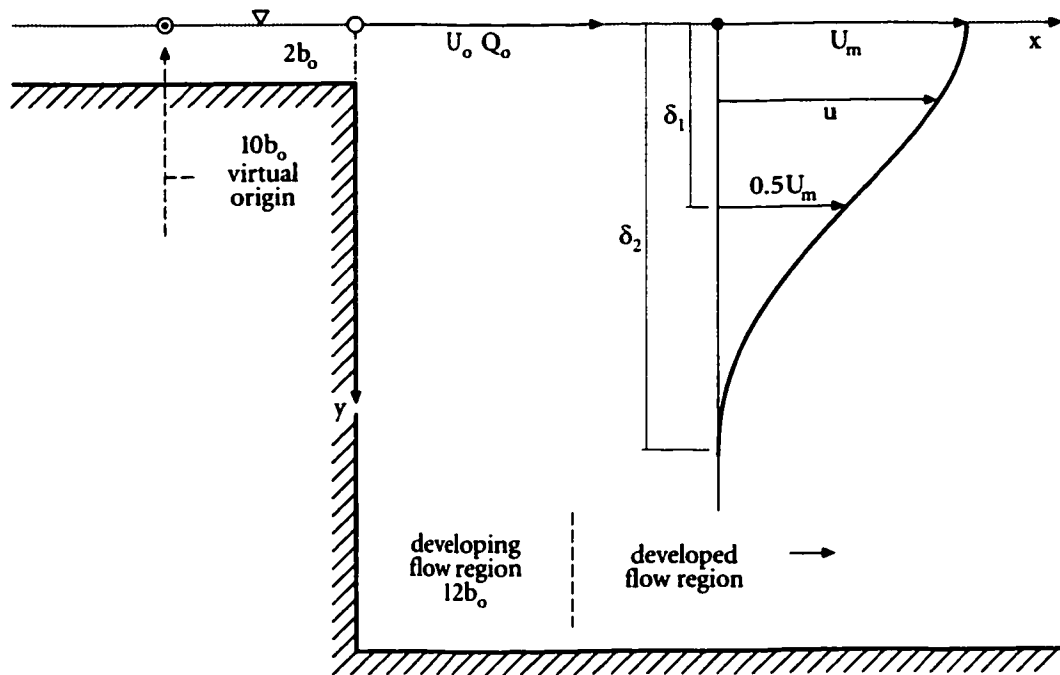


Figure 2.5: Plane turbulent surface jet definition sketch.

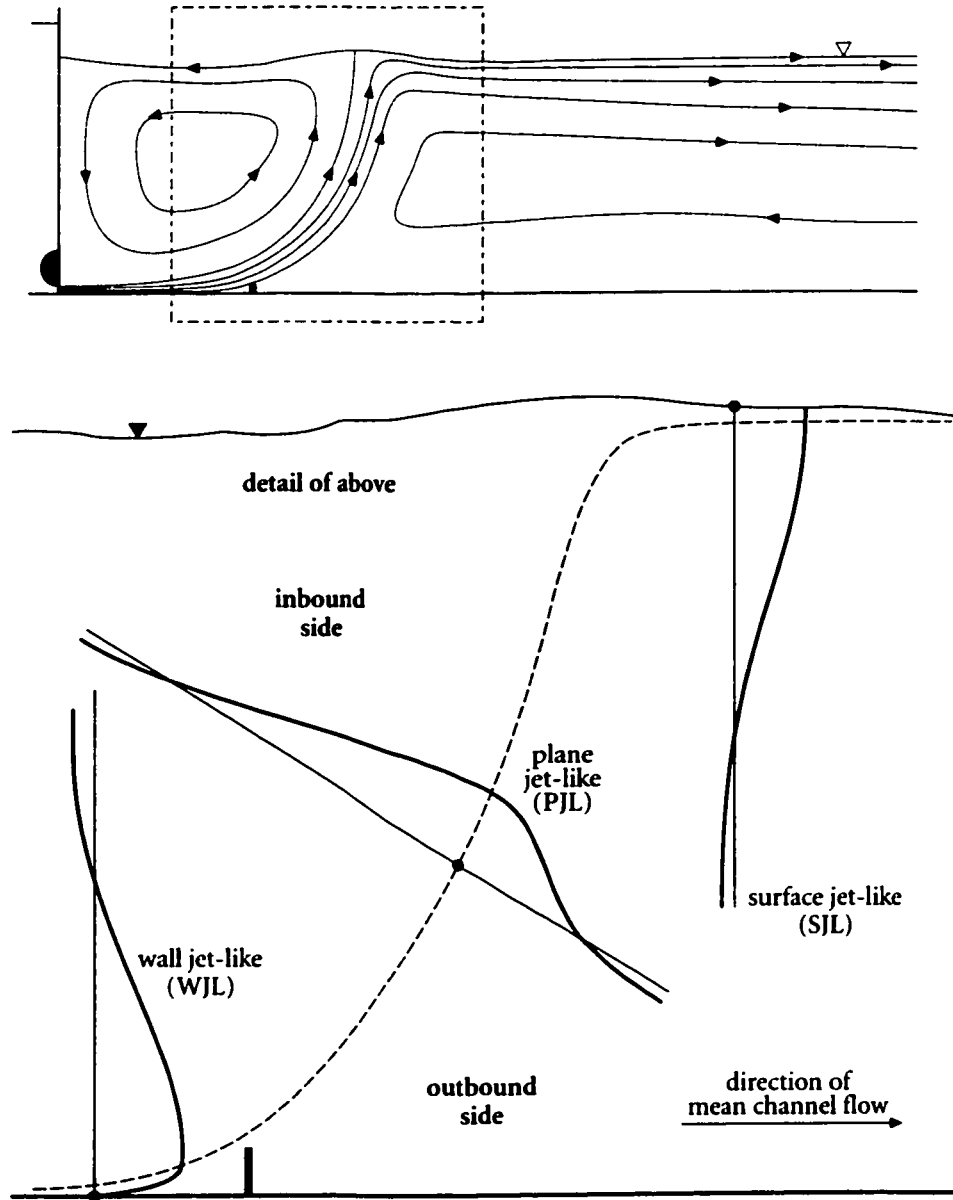


Figure 2.6: Plane deflected wall jet definition sketch.

3 Experimental Methods

The particle image velocimetry (PIV) technique used in this experimental work requires a complex instrumentation arrangement and data analysis programme in addition to a modified physical flow setup. This section is divided into four main subsections: §3.1 outlines basic PIV methodology, §3.2 describes the flume arrangement, §3.3 presents the PIV setup assembly and §3.4 describes the measurement programme.

3.1 PIV Methodology

Particle image velocimetry is a technique which employs tracer particles suspended in a flow to provide a quantitative measure of the instantaneous velocity field of the flow (Prasad *et al.* 1992). Generally, a plane section of a flow is illuminated by a light source and a sequence of images is recorded with a specified time interval between images. The resulting image sequence captures specular reflections from the seeded particles as they travel in the illuminated flow plane. If the timing sequence of the illumination and recording processes are synchronized correctly, and if the majority of particles remain in the illuminated field of view (FOV) without appreciable out-of plane-motion particle loss, individual particles or patterns of particles can be tracked between images. With knowledge of the time separation between the images, correlations, displacements and hence velocities can then be computed for either individual particles or for regions encompassing groups of particles.

In the earliest PIV methods, particles carried by a flow were imaged under natural light onto photographic film and velocity data extracted through manual displacement measurement. Artificial, and strobing illumination devices were later introduced to increase image quality and decrease minimum time separations, including illumination by laser light. Variations on the classic photographic PIV method, including double exposures within single images, were used in order to reduce both the number of images analyzed and the cost associated with photo development. Computers aided in the analysis if images were digitized and processed. As charge-coupled device (CCD) camera technology matured and powerful computers became more readily available, completely digital PIV analysis methods followed. An excellent review of PIV theory and history is presented by Raffel *et al.* in the book *Particle Image Velocimetry: A Practical Guide* (1998) and by Lourenço (1996).

The PIV technique implemented in this current work employs reflective tracer particles, a pulsing laser sheet and various digital devices to produce, store and process image sequences. These sequences are separated into image pairs which are then processed by computer to obtain cross-correlation fields and ultimately, instantaneous velocity fields. A detailed description of the actual PIV computational process which extracts the velocity data from the images is presented in §4.

3.2 Flume Arrangement

The experiments presented in this study were conducted in the T. Blench Hydraulics Laboratory, at the University of Alberta in Edmonton, Canada. A relatively large rectangular flume with a self-contained water supply, as shown in Figure 3.1, was employed. The horizontal under-bed of the flume was constructed of aluminium, topped with either Plexiglas or glass, and the sidewalls were also either Plexiglas or glass. An aluminium baffle was located downstream of the channel gate and placed across the width of the flume and perpendicular to the centreline. There was a rectangular opening in the aluminium under-bed, aligned with the centreline axis of the flume, situated to allow unobstructed transmission of the laser sheet through the channel bed and into the flow. Due to the scratched and clouded condition of the Plexiglas sidewalls, glass was installed where greater clarity and transparency was required for both image capture and laser transmission. Flume covers and sidewall shrouds were employed to eliminate ambient light pollution of the PIV imaging area. Water was pumped from the downstream reservoir into the upstream head tank with discharge measured by a magnetic flowmeter located in the supply line.

The global Cartesian coordinate system of the flume assembly has an origin defined at the downstream gate section, at the flume bed and in the centre of the channel width. The definition and direction of the coordinate axes are identical to those of the classical plane turbulent wall jet, i.e. x was the longitudinal coordinate, y was the vertical coordinate and z was the transverse coordinate.

The channel itself measured 45.7 cm wide, 450.0 cm long and 90.2 cm tall and was raised 95.3 cm above the floor, allowing for piping and PIV equipment to be placed under the channel bed. Figure 3.2 is a dimensioned drawing of the channel. Water enters the flume from the head tank under a sluice gate with a streamlined lip, and produces a supercritical stream of thickness equal to the slot width of the gate opening. Both the slot width b_o and the baffle height h_o were set at 2.54 cm for the experiments discussed in this work. The tailwater level was controlled via an adjustable weir located at the downstream end of the flume. The baffle consists of a 3.175 mm thick aluminium angle (painted black to eliminate reflections), affixed to the bed at $x_o = 50.0$ cm downstream of the sluice gate opening, with the vertical face of the angle facing upstream. A section of the angle bottom at the centreline of the flume was removed so that the baffle provided the least possible obstruction to the laser illumination sheet. When the pump was in operation and the reservoir fully filled, the flume arrangement held approximately 8 m³ of water. This water was seeded with approximately 30 g of silver-coated glass sphere tracer particles (Potter Industries, Valley Forge, Pennsylvania) with a 15 μ m nominal diameter and a mean specific gravity of 2.6.

3.3 PIV Setup

The PIV instrumentation used in this study of the plane deflected wall jet was comprised of three main sub-systems: the illumination system, consisting of a laser and optics; the timing system, consisting of a signal sync stripper and a delay generator; and the imaging system, consisting of a CCD camera, a computer equipped with a frame-grabber and a positioning and targeting apparatus. The three sub-systems were configured to sample sequential digital images of the seeded flow, capturing pairs separated by small Δt values at an ultimate rate of 15 Hz. Figure 3.3 shows (a) the general layout of the PIV setup and (b) laser timing structure.

3.3.1 Illumination Sub-System

The central element of the illumination sub-system was the laser. It was used to produce a beam of light that, when directed through a plano-cylindrical lens, was spread into a sheet of light the same thickness as the beam. The laser was fastened to a mobile table equipped with an optical rail; the laser was fixed so that the axis of the beam follows the rail and was perpendicular to the flume. The plano-cylindrical lens was attached to the rail and aligned such that the beam passed through the lens centre to produce a plane of light parallel to the flume bed. The mobile table height was adjusted so the horizontal light sheet passed under the lower edge of the flume and a mirror angled at 45 degrees was used to reflect it vertically upwards through the glass bed and into the channel. This sheet illuminates a plane in the flow along the centreline of the channel, coincident with the x-y plane of the flume. Figure 3.4 shows a diagrammatic representation of the illumination sub-system.

The specific laser used in this study was a dual-cavity Minilite PIV model q-switched Nd:YAG laser (Continuum Electro-Optics, Santa Clara, California). Along with internal optics, electrical components and a distilled-water cooling system, each laser cavity contains a flashlamp and a solid-state lasing-medium rod. The two rods are called laser A and laser B for convenience. Both lasers are housed in a single laser head, and beams from each cavity are tuned to be co-incident upon emission. When electrically stimulated by the power supply, the flashlamp emits a non-polarized light which excites the Neodymium atoms in the rod. These atoms absorb and effectively store the flashlamp's optical energy until the rod is allowed to release the energy. The release of the laser energy, expressed as a highly coherent laser-light beam, occurs a short time (defined as the build-up time) after the q-switch component of the laser is triggered and opened. Thus the beam generation and emission of each Minilite PIV laser cavity is controlled via two different signals: the flashlamp delay and the q-switch delay. The sequence and cycle pattern of the resulting four delay signals directly controls the timing and strength of the dual laser pulses.

The Nd:YAG laser produces horizontally polarized infrared light at a wavelength of 1064 nm by default, but with the installation of non-linear crystals and dichroics, wavelengths of 532 nm, 355 nm, and 266 nm can also be produced. In this experiment,

the laser operated at the visible wavelength of 532 nm to produce a circularly polarized beam of 3 mm nominal diameter. Under such operating conditions, the lasers each achieve 28 mJ per pulse, resulting in an average power level of 0.42 W per laser rod. The combined energy was 56 mJ per each dual-pulse, resulting in a total power level of 0.84 W. Separation time (Δt) between pulses could vary between 40 ns and 100 ms. The rated build-up time was 60 ns and the rated pulse width was approximately 5 ns. Factory calibrations indicated that to achieve optimal power in each laser, the q-switch delay should be set to 148 μ s, however it was found that lasers A and B required individual and unique q-switch delays to produce pulses of equal intensity.

The plano-cylindrical glass lens (Melles-Griot, Nepean, Ontario) had a focal length of -12.7 mm and a design wavelength of 587.6 nm. The flat surface mirror (Edmund Industrial Optics, Barrington, New Jersey) was 200 mm by 235 mm in size and was comprised of a fine annealed Pyrex substrate coated with enhanced aluminium as protection and to increase reflectance in the 200 nm to 650 nm range. These optics produced a pulsed 3 mm thick light sheet that can be directed upwards, perpendicular to the flume bed, and positioned perfectly along the centreplane of the flow.

3.3.2 Timing Sub-System

In order to synchronize the laser pulses with the imaging system, and to enable use of the PIV technique, the laser pulses must be accurately controlled. This is accomplished by the timing sub-system. The purpose of the timing sub-system is to produce pulses of illumination very close to the end of the first frame of an image pair and very close to the beginning of the second frame of the same pair. It must do this repeatedly, as long as images are being acquired by the imaging sub-system. In this way high-velocity flows can be resolved using standard 30 Hz digital video equipment. The main timing component was a model 500A (Berkeley Nucleonics, San Rafael, California) pulse generator. It has one input BNC connection and four BNC output connections.

Using an external input signal as a trigger, it generates four separate output signals with user-programmable delays, pulse widths and polarities. The delays generated by the four outputs are called T1, T2, T3 and T4 respectively. They correspond to the laser A flashlamp and q-switch delays (T1 and T2) and the laser B and flashlamp and q-switch delays (T3 and T4) previously discussed. With the exception of the T2 delay, each is triggered by the same rising edge in the input signal. T2 is triggered at the end of the T1 signal. The input signal to the delay generator was a 15 Hz square signal describing the occurrence rate of image pairs. This signal was derived from the 30 Hz odd-even signal stripped from the analog video output of the CCD camera using a video signal sync stripper circuit assembled at the University of Alberta. The sync stripper produces a signal with a rising edge at the beginning of every second frame taken by the imaging system. Figure 3.5 (a) presents a schematic diagram of the timing sub-system connection and signal flow and Figure 3.5 (b) illustrates the detailed timing scheme.

3.3.3 Imaging Sub-System

The imaging sub-system is responsible for the storage and acquisition of the digital PIV images. It is comprised of a digital CCD camera, a desktop computer equipped with a digital frame-grabber, image acquisition software and a positioning and targeting apparatus. The camera signal drives the PIV imaging as well as provides the necessary input to the timing sub-system. The camera used for imaging was a model TM-1040 progressive scanning high resolution monochrome CCD camera (Pulnix, Sunnyvale, California) with a 30 fps output rate. It captures 10-bit grayscale images 1 008 px by 1 008 px in size and has an adjustable manual gain control. Both digital and analog output is provided. Equipped with a 25 mm 1:1.4 camera lens (Fujinon, Deerfield, Illinois) and set at an aperture of 2.8, the camera has a approximate minimum 9 cm FOV length.

Digital images were recorded using a single 733 MHz Pentium III-class personal computer running Windows NT 4, equipped with 256 MB of RAM memory and a striped-set array of four high-speed SCSI 9.1 GB (unformatted) hard drives as well as a removable hard drive bay. The frame-grabbing software package Video Savant (IO Industries, London, Ontario) and Road Runner digital camera interface hardware (BitFlow, Woburn, Massachusetts) permitted real-time image acquisition to the computer and subsequent export of individual image frames in an 8-bit tagged image file format (TIFF) for further analysis. A maximum of approximately 34 000 frames could be captured to the striped-set array before export to the removable hard drive was required.

Through early experimental investigation using acoustic Doppler velocimetry (ADV), it was decided that the complete field of interest of the plane deflected wall jet phenomenon began approximately 35 cm downstream of the gate and extended approximately 60 cm further downstream. Because actual pixel (px) resolution is reduced when larger fields of view are employed (i.e. each pixel element represents and reduces to a single grayscale value a larger physical area), the area was divided into tesserae which could be imaged separately and later combined into one complete mosaic. This led to the need for accurate positioning of the camera in the global coordinate system. Such a system was provided through use of a positioning stage for the camera and a corresponding target apparatus placed in the flume at the location of the particular tessera FOV. The camera was attached to a set of precision scissor-jacks which controlled the vertical height of the camera. A small two-dimensional stage was installed between the upper jack and the camera to provide accurate positioning in the horizontal plane. This entire assembly was supported by a table constructed so as not to interrupt the path of the laser.

The target apparatus consisted of rigid 75 cm by 100 cm Lexan sheet placed into the operating flume and locked into position through the use of spacer bars, clamps and wedges. The target apparatus was placed on the flume bed at the centreline, so that the grid plane was coincident with both the laser sheet and the focused FOV of the

camera. During the course of the experiment, the target would be lowered into the flow, and the laser and camera positioned to provide illumination and imaging for the tessera of interest before data was collected. A laminated 1-cm grid was created and adhered to the rigid sheet to provide tesserae reference points. Sixteen overlapping square tesserae formed the single square mosaic: each tessera 15.75 cm by 15.75 cm in size, with 0.75 cm overlaps, resulting in a mosaic 60.75 cm by 60.75 cm in size. Tesserae centres, edges and numbers were visible during setup and allowed the camera to be consistently positioned in the global coordinate system via optical adjustment. Figure 3.6 shows a dimensioned drawing of the target apparatus in relation to the flume and baffle.

Figures 3.7 through 3.14 show photographs taken of the complete experimental area, including the flume arrangement and the PIV setup sub-systems.

3.4 Measurement Programme

Fourteen of the available sixteen tesserae were chosen to adequately describe the plane deflected wall jet and the follow the jet centreline trajectory and are shown in Figure 3.6 as the numbered tesserae. The data collection programme began at the fourteenth tessera and then proceeded in an order chosen to reduce equipment movement and repositioning. The exact location of the target and alignment apparatus was set so the baffle was always centered in the overlap region between the second and third tesserae. This minimized the manifestation of a baffle shadow in the captured images to a thin wedge-like region above the baffle. Table 3.1 presents the global coordinate centres and extents of the individual tesserae FOV areas. The lowest image edge is not found at the bed due to the visible presence of silicon caulking at the flume seams and because of reflections at the glass bed boundary. The image scale is $S_{\text{FOV}} = 156.25 \mu\text{m/px}$.

The flow rate in the flume was measured by a voltmeter connected to the magnetic flowmeter; the average reading was 30.6 volts, corresponding to an average volumetric flow rate of $Q = 0.0153 \text{ m}^3/\text{s}$, a discharge intensity of $q = 0.0335 \text{ m}^2/\text{s}$, and a mean uniform jet exit velocity of $U_o = 1.32 \text{ m/s}$. The resulting average Reynolds and Froude numbers were $R = 28\,400$ and $F = 2.64$, respectively. The average tailwater depth y_1 and depth immediately downstream of the gate y_2 were both 55.0 cm while the average depth immediately upstream of the gate in the head tank was $y_1 = 64.0 \text{ cm}$. The U_o measurement from the flowmeter was confirmed using the relation $U_o = \sqrt{2g\Delta H} = 1.33 \text{ m/s}$. A mean water surface profile was taken through direct measurement of the water level at the flume sidewall; profile data is presented in Table 3.2. The experimental work was completed over an approximate ten-hour period over which the average measured water temperature was 13.8 °C, yielding a mean kinematic viscosity of $\nu = 0.0118 \text{ cm}^2/\text{s}$. The electronic thermometer used in temperature measurement broke after the tessera 8 data collection process. Temperatures for the tesserae 9 through 13 experiments were calculated by averaging

the temperatures from tesserae 4 through 8 experiments. The water temperature while collecting data for tessera 14 was 10.8 °C and it stabilized at approximately 14.0 °C by the tessera 4 experiment. Only actually measured temperatures were included in the average calculation. The full set of environmental data is provided in Table 3.3.

The laser timing and delays for each tessera were programmed individually and recalled from the delay generator memory before data collection commenced at each section. The Δt pulse separations were chosen based on a maximum allowable particle pixel shift of 16 px in either the x- or y-direction and a maximum expected instantaneous velocity for the individual tesserae as measured in both the investigatory ADV study and preliminary PIV measurements. The need for this limitation is made clear in §4 and is related to the size of the chosen interrogation window in the PIV analysis. The minimum pulse separation was 1.3 ms, corresponding to a maximum instantaneous velocity resolution of 192 cm/s; the maximum pulse separation was 4.0 ms, corresponding to a minimum instantaneous velocity resolution of 63 cm/s. The full set of delays and pulse separations are presented in Table 3.4 with a sample calculation provided in §8.

A total of 180.2 seconds of 30 frames per second (fps) video data was recorded for each of the tesserae. This corresponds to 5 400 TIFF flawless images per tessera and 76 600 flawless images for the complete experimental mosaic. In addition, images were taken of the target apparatus to confirm location and scale accuracy. Figure 3.15 shows the target images for tesserae (a) twelve and (b) thirteen; note the centre point, the cm-grid, the FOV edges and the water surface. Each TIFF image is approximately 0.97 MB in size; this necessitated periodic export of image data from the main PIV hard drive to one of three 60 GB (unformatted) removable hard drives. The first hard drive stored the images of tesserae 14, 1, 2 and 3; the second hard drive stored the images of tesserae 4, 5, 6, 7 and 8; and the third hard drive stored the images of tesserae 9, 10, 11, 12 and 13. The average time to export the images of one tessera to the removable media was approximately 25 minutes. All three drives were less than half full in anticipation of further processing and data-file creation.

tessera	x-centre (cm)	y-centre (cm)	top (cm)	bottom (cm)	left (cm)	right (cm)
1	42.625	23.125	31.00	15.25	34.75	50.50
2	42.625	8.125	16.00	0.25	34.75	50.50
3	57.625	8.125	16.00	0.25	49.75	65.50
4	57.625	23.125	31.00	15.25	49.75	65.50
5	57.625	38.125	46.00	30.25	49.75	65.50
6	57.625	53.125	61.00	45.25	49.75	65.50
7	72.625	53.125	61.00	45.25	64.75	80.50
8	72.625	38.125	46.00	30.25	64.75	80.50
9	72.625	23.125	31.00	15.25	64.75	80.50
10	72.625	8.125	16.00	0.25	64.75	80.50
11	87.625	23.125	31.00	15.25	79.75	95.50
12	87.625	38.125	46.00	30.25	79.75	95.50
13	87.625	53.125	61.00	45.25	79.75	95.50
14	42.625	38.125	46.00	30.25	34.75	50.50

Table 3.1: Global coordinate tesserae positions and extents.

x (cm)	y (cm)	x (cm)	y (cm)	x (cm)	y (cm)
10.0	54.1	48.0	52.5	86.0	54.3
11.0	54.1	49.0	52.4	87.0	54.3
12.0	54.1	50.0	52.5	88.0	54.1
13.0	54.1	51.0	52.6	89.0	54.1
14.0	54.2	52.0	52.9	90.0	54.0
15.0	54.0	53.0	53.1	91.0	54.0
16.0	53.9	54.0	53.3	92.0	53.9
17.0	53.9	55.0	53.2	93.0	53.9
18.0	53.7	56.0	53.3	94.0	53.9
19.0	53.5	57.0	53.3	95.0	53.8
20.0	53.3	58.0	53.5	96.0	53.7
21.0	53.3	59.0	53.9	97.0	53.7
22.0	53.1	60.0	54.0	98.0	53.6
23.0	52.9	61.0	53.9	99.0	53.6
24.0	52.9	62.0	54.0	100.0	53.6
25.0	52.9	63.0	54.1	101.0	53.5
26.0	52.8	64.0	54.3	102.0	53.5
27.0	52.8	65.0	54.5	103.0	53.5
28.0	52.7	66.0	54.5	104.0	53.5
29.0	52.7	67.0	54.7	105.0	53.5
30.0	52.6	68.0	54.9	106.0	53.4
31.0	52.6	69.0	55.0	107.0	53.5
32.0	52.6	70.0	55.1	108.0	53.3
33.0	52.7	71.0	55.0	109.0	53.3
34.0	52.8	72.0	54.9	110.0	53.4
35.0	52.7	73.0	54.9	111.0	53.5
36.0	52.6	74.0	54.8	112.0	53.5
37.0	52.7	75.0	54.7	113.0	53.5
38.0	52.5	76.0	54.7	114.0	53.6
39.0	52.5	77.0	54.7	115.0	53.6
40.0	52.4	78.0	54.6	116.0	53.7
41.0	52.3	79.0	54.6	117.0	53.6
42.0	52.3	80.0	54.8	118.0	53.8
43.0	52.3	81.0	54.7	119.0	53.9
44.0	52.5	82.0	54.7	120.0	54.0
45.0	52.7	83.0	54.6	-	-
46.0	52.7	84.0	54.6	-	-
47.0	52.7	85.0	54.5	-	-

Table 3.2: Mean water surface profile coordinates.

tessera	V (volts)	Q (m ³ /s)	U _o (cm/s)	T (°C)	v (cm ² /s)	γ ₁ (cm)	γ ₂ (cm)	γ _t (cm)
1	30.8	0.0154	132.6	11.8	0.0125	64.0	55.0	55.0
2	30.8	0.0154	132.6	12.1	0.0124	64.0	55.0	55.0
3	30.6	0.0153	131.8	12.4	0.0123	64.0	55.0	55.0
4	30.8	0.0154	132.6	14.0	0.0117	64.0	55.0	55.0
5	30.3	0.0152	130.5	16.0	0.0111	64.0	55.0	55.0
6	30.5	0.0153	131.3	14.6	0.0115	64.0	55.0	55.0
7	30.6	0.0153	131.8	14.3	0.0116	64.0	55.0	55.0
8	30.9	0.0155	133.0	14.2	0.0117	64.0	55.0	55.0
9	30.3	0.0152	130.5	14.6 *	0.0115	64.0	55.0	55.0
10	30.6	0.0153	131.8	14.6 *	0.0115	64.0	55.0	55.0
11	30.6	0.0153	131.8	14.6 *	0.0115	64.0	55.0	55.0
12	30.5	0.0153	131.3	14.6 *	0.0115	64.0	55.0	55.0
13	30.6	0.0153	131.8	14.6 *	0.0115	64.0	55.0	55.0
14	30.8	0.0154	132.6	10.8	0.0128	64.0	55.0	55.0
average	30.6	0.0153	131.8	13.8	0.0118	64.0	55.0	55.0

notes: laser A flashlamp delay = 148 μs and laser B flashlamp delay = 228 μs
laser A and laser B q-switch delay = 63 ns

* indicates interpolated temperature data not use in average

Table 3.3: Environmental parameters.

tessera	Δt (ms)	T1 delay (s)	T2 delay (s)	laser A pulse (s)	T3 delay (s)	T4 delay (s)	laser B pulse (s)
1	3.0	0.0151666	0.0001480	0.0153147	0.0180866	0.0183146	0.0183147
2	1.3	0.0160166	0.0001480	0.0161647	0.0172366	0.0174646	0.0174647
3	1.6	0.0158666	0.0001480	0.0160147	0.0173866	0.0176146	0.0176147
4	1.7	0.0158166	0.0001480	0.0159647	0.0174366	0.0176646	0.0176647
5	2.0	0.0156666	0.0001480	0.0158147	0.0175866	0.0178146	0.0178147
6	2.0	0.0156666	0.0001480	0.0158147	0.0175866	0.0178146	0.0178147
7	2.0	0.0156666	0.0001480	0.0158147	0.0175866	0.0178146	0.0178147
8	1.8	0.0157666	0.0001480	0.0159147	0.0174866	0.0177146	0.0177147
9	1.7	0.0158166	0.0001480	0.0159647	0.0174366	0.0176646	0.0176647
10	3.0	0.0151666	0.0001480	0.0153147	0.0180866	0.0183146	0.0183147
11	4.0	0.0146666	0.0001480	0.0148147	0.0185866	0.0188146	0.0188147
12	2.6	0.0153666	0.0001480	0.0155147	0.0178866	0.0181146	0.0181147
13	2.0	0.0156666	0.0001480	0.0158147	0.0175866	0.0178146	0.0178147
14	2.6	0.0153666	0.0001480	0.0155147	0.0178866	0.0181146	0.0181147

notes: laser A flashlamp delay = 148 μ s and laser B flashlamp delay = 228 μ s
laser A and laser B q-switch delay = 63 ns

Table 3.4: Experimental timing delays and separations.

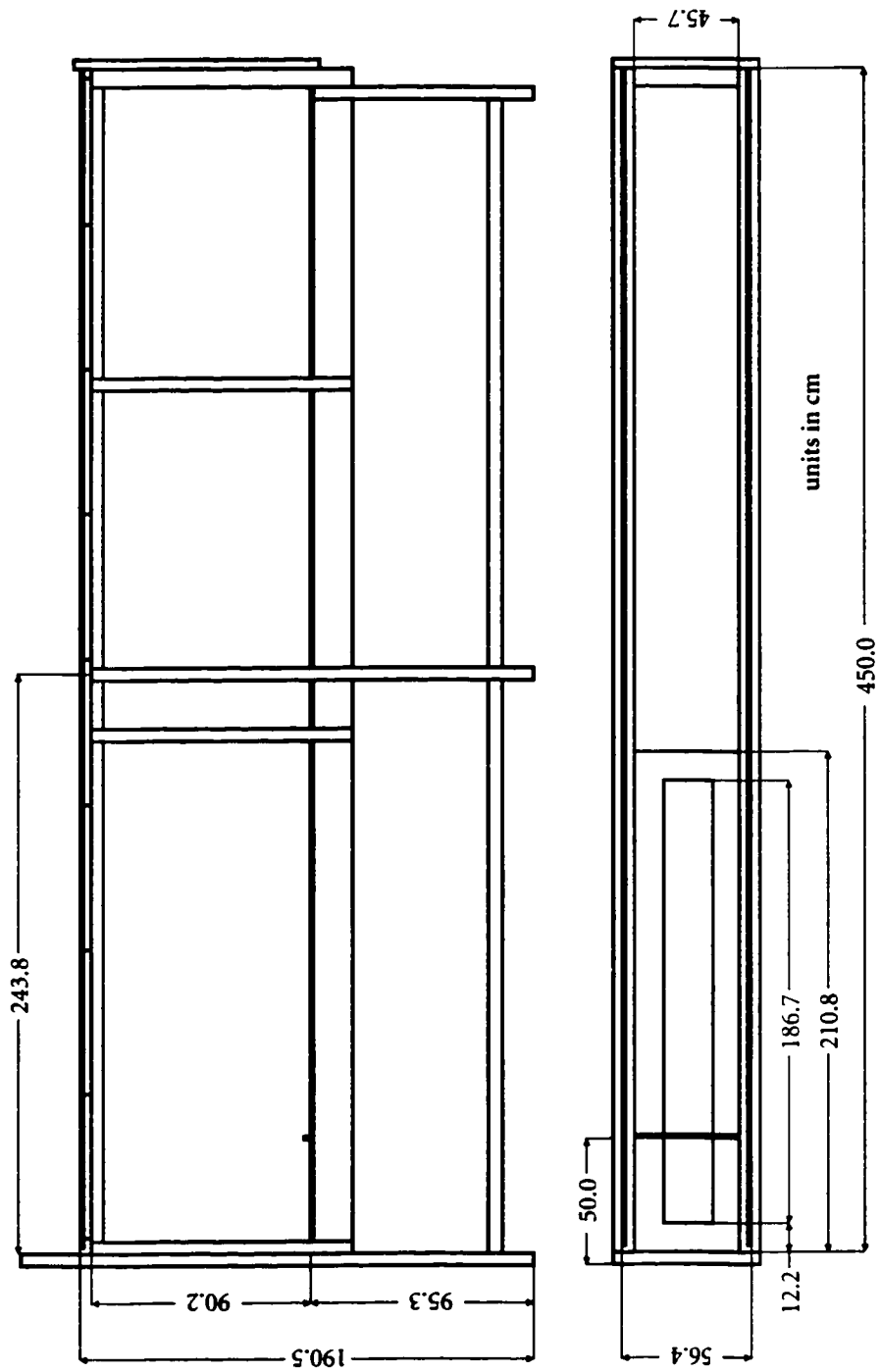


Figure 3.2: Channel measured drawing.

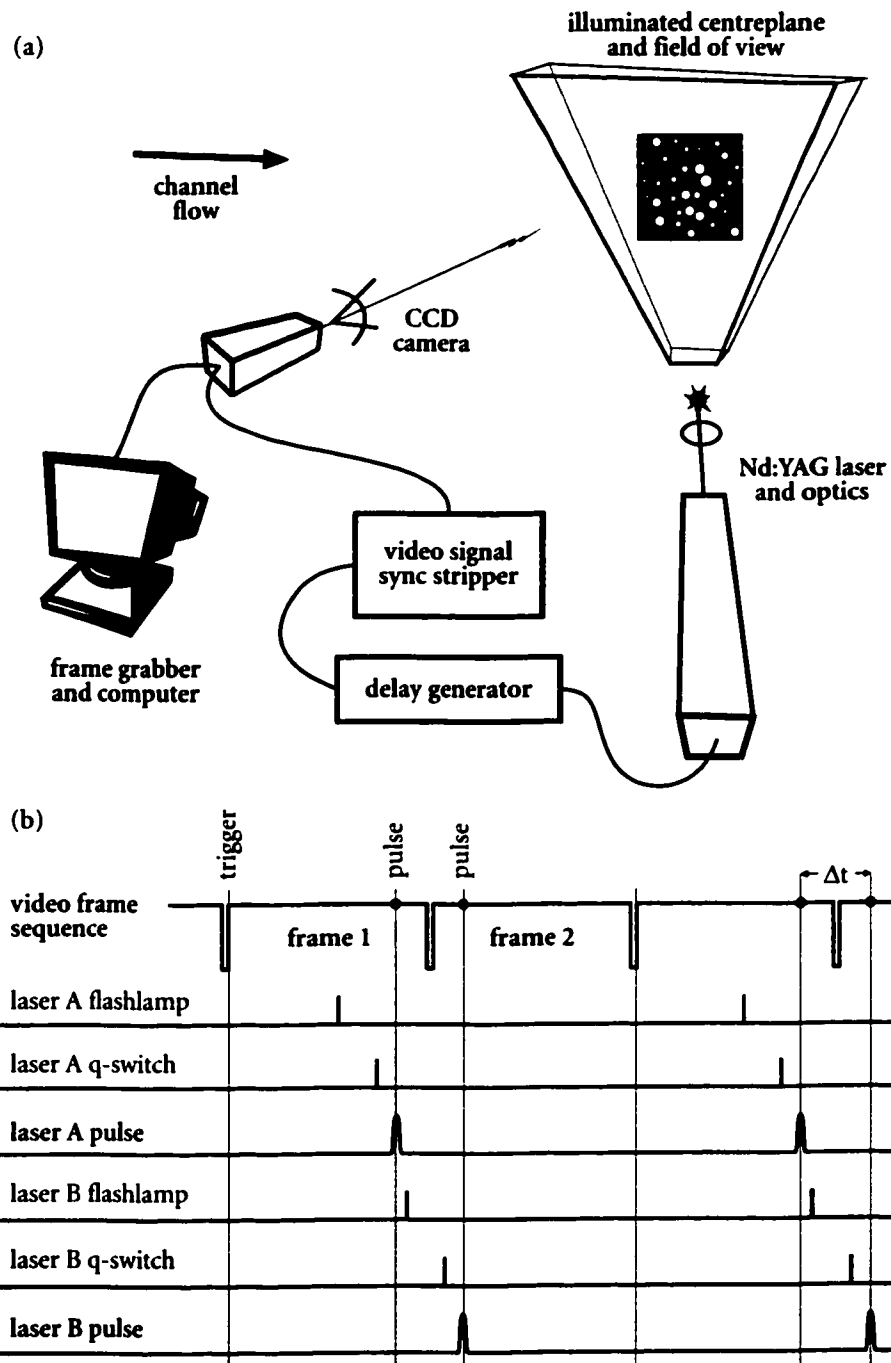


Figure 3.3: (a) General PIV setup layout and (b) broad laser timing structure.

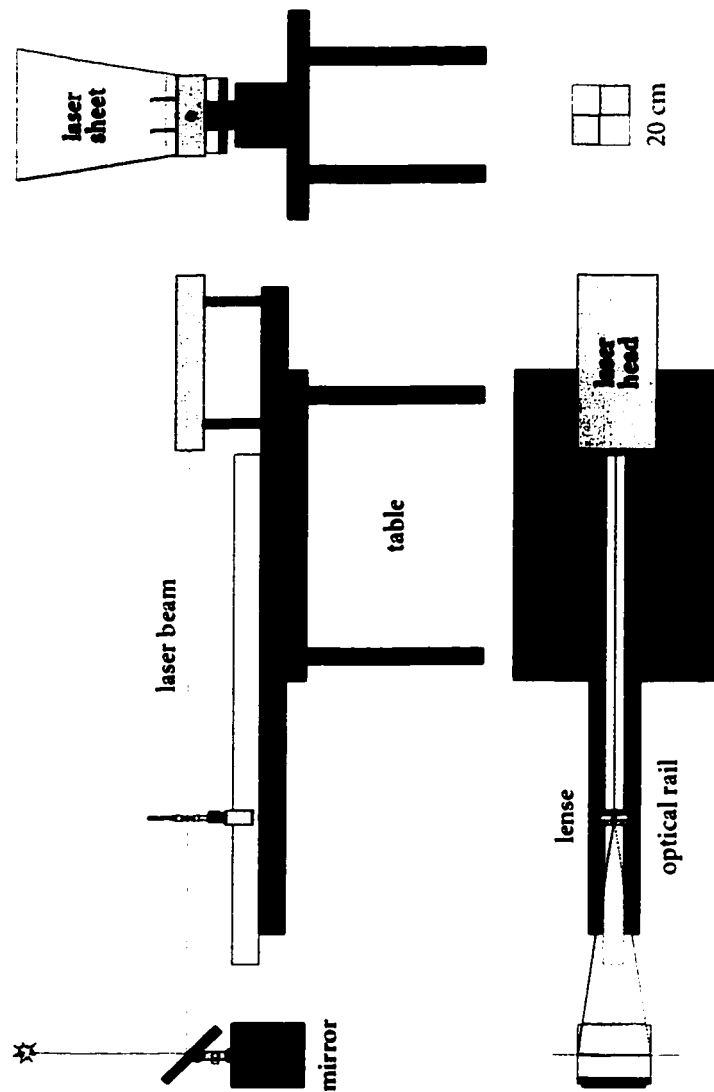


Figure 3.4: PIV illumination sub-system diagram.

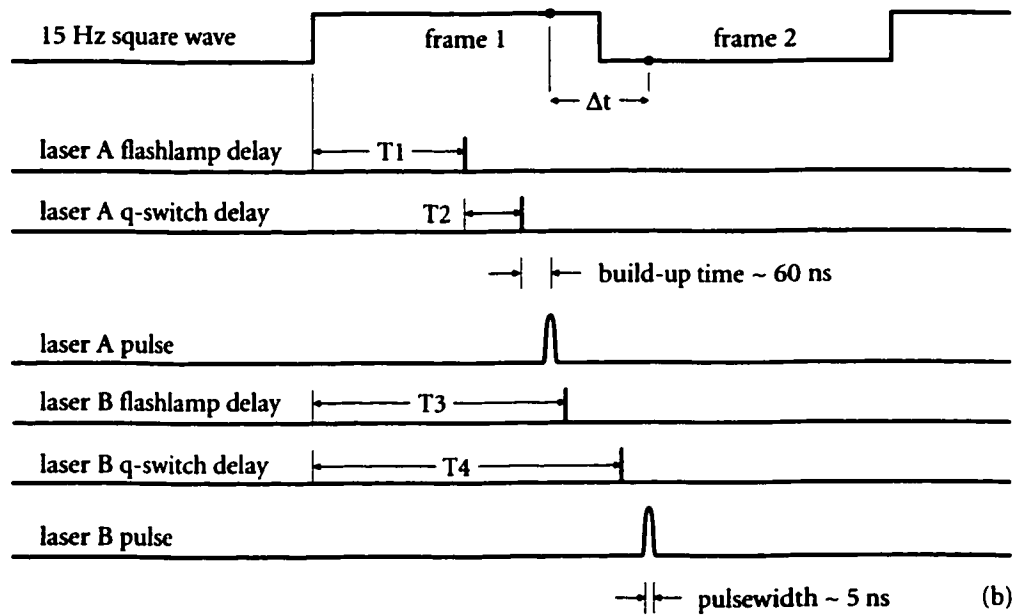
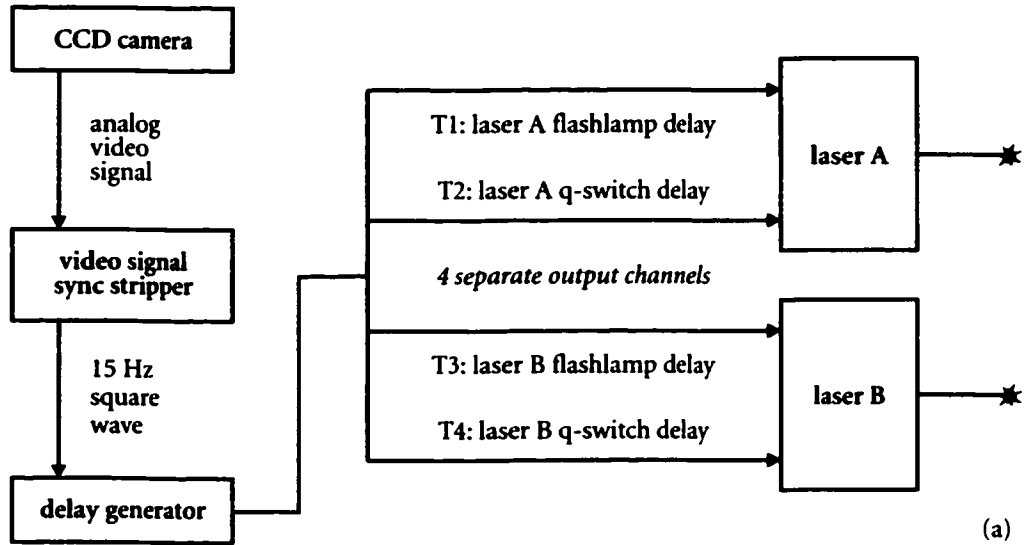


Figure 3.5: (a) PIV timing sub-system signal flow and (b) detailed timing scheme.

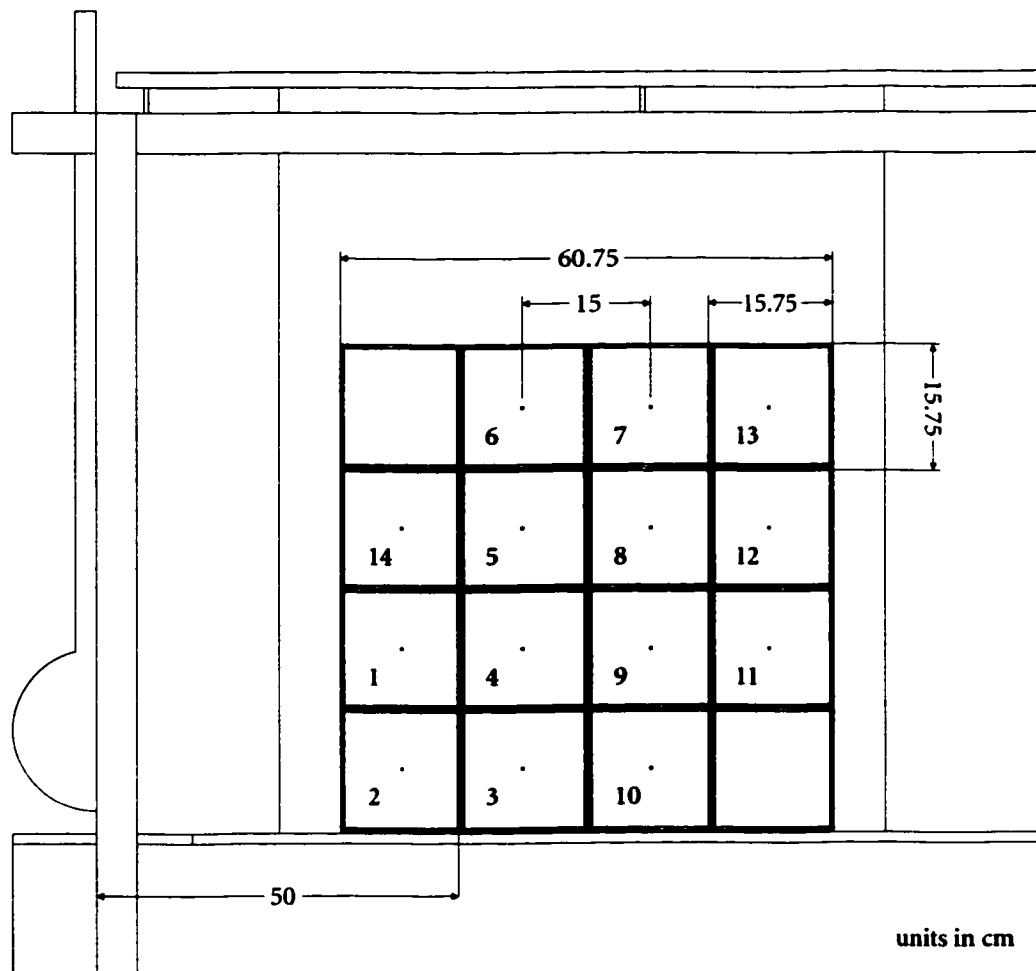


Figure 3.6: PIV imaging sub-system target apparatus measured drawing.